- 1 Title: Cholinergic Modulation Shifts the Response of CA1 Pyramidal Cells to Depolarizing Ramps via
- 2 TRPM4 Channels with Potential Implications for Place Field Firing

3

4 Abbreviated Title: Cholinergic Modulation Shifts the Response of CA1 Pyramidal Cells

5

- Author Names and Affiliations: Crescent Combe¹, Carol Upchurch², Carmen C. Canavier^{2*} and Sonia 6
- Gasparini^{1,2}* 7
- ¹Neuroscience Center of Excellence, and ²Department of Cell Biology and Anatomy, School of Medicine, 8
- 9 Louisiana State University Health Sciences Center, New Orleans, Louisiana, USA 70112

10

11 * these authors jointly supervised this work

12

- 13 Corresponding author: Sonia Gasparini, Neuroscience Center, Louisiana State University Health
- 14 Sciences Center, New Orleans, 2020 Gravier St., New Orleans, LA 70112, sgaspa1@lsuhsc.edu

15

- 16 Number of pages: 41
- 17
- Number of figures: 11 (+ 3 supplemental figures)
- 18 Conflict of interest statement: The authors declare no competing financial interests.

19

- 20 Acknowledgements: This work was funded by NIH R01 MH115832 under the CRCNS program to SG
- and CCC and by the Research Enhancement Program of the School of Medicine at the Louisiana State 21
- 22 University Health Sciences Center to SG. The simulations utilized resources provided by NSF 2018936.
- 23 We would like to thank Drs. Christopher Del Negro, Barbara Ehrlich and Dan Johnston for helpful
- 24 discussions.

Abstract

25

26

27

28

29

30

31

32

33

34

35

36

37

38

39 40

41 42 A synergistic combination of in vitro electrophysiology and multicompartmental modeling of rat CA1 pyramidal neurons identified TRPM4 channels as major drivers of cholinergic modulation of the firing rate during a triangular current ramp, which emulates the bump in synaptic input received while traversing the place field. In control, fewer spikes at lower frequencies are elicited on the down-ramp compared to the up-ramp due to long-term inactivation of the Na_V channel. The cholinergic agonist carbachol (CCh) removes or even reverses this spike rate adaptation, causing more spikes to be elicited on the downramp than the up-ramp. CCh application during Schaffer collateral stimulation designed to simulate a ramp produces similar shifts in the center of mass of firing to later in the ramp. The non-specific TRP antagonist flufenamic acid and the TRPM4-specific blockers CBA and 9-phenanthrol, but not the TRPCspecific antagonist SKF96365, reverse the effect of CCh; this implicates the Ca²⁺-activated nonspecific cation current, I_{CAN}, carried by TRPM4 channels. The cholinergic shift of the center of mass of firing is prevented by strong intracellular Ca²⁺ buffering but not by antagonists for IP₃ and ryanodine receptors, ruling out a role for known mechanisms of release from intracellular Ca²⁺ stores. Pharmacology combined with modeling suggest that [Ca2+] in a nanodomain near the TRPM4 channel is elevated through an unknown source that requires both muscarinic receptor activation and depolarization-induced Ca2+ influx during the ramp. Activation of the regenerative inward TRPM4 current in the model qualitatively replicates and provides putative underlying mechanisms for the experimental observations.

Introduction

43

- 44 Release of the neuromodulator acetylcholine is thought to be correlated with certain brain states or
- 45 functions (Pepeu and Giovannini, 2004). In the hippocampal formation, elevated acetylcholine is
- 46 associated with exploration (Bianchi et al., 2003), particular memory processes (Micheau and Marighetto,
- 47 2011), REM sleep (Hutchison and Rathore, 2015), and response to novelty (Acquas et al., 1996; Thiel et
- 48 al., 1998; Giovannini et al., 2001).
- 49 The major cholinergic input to the hippocampus is from the medial septum and diagonal band of Broca,
- which innervate all hippocampal subfields (Dutar et al., 1995). As for the degree to which acetylcholine
- release is spatially targeted, this is still under debate (Disney and Higley, 2020; Sarter and Lustig, 2020);
- 52 however it has been shown that CA1 receives cholinergic afferents in all layers, although at different
- 53 densities (Nyakas et al., 1987; Aznavour et al., 2002). Pyramidal neurons express G-protein-coupled
- 54 metabotropic muscarinic acetylcholine receptors (mAChRs) (Levey et al., 1995), more so than they do
- 55 ionotropic (nicotinic) receptors, which are primarily on interneurons in this region (Dani and Bertrand.
- 56 2007). M₁ mAChRs, in particular, are found on both dendritic shafts and spines of CA1 pyramidal
- 57 neurons (Yamasaki et al., 2010).
- 58 Elevated acetylcholine in the hippocampal formation is thought to favor memory encoding, and
- 59 modulates theta oscillations (Hasselmo, 2006), which in turn modulate place cell firing (Easton et al.,
- 60 2012). There is evidence that cholineraic activity regulates long-term synaptic plasticity (Huerta and
- 61 Lisman, 1995; Palacios-Filardo and Mellor, 2019; Fernández de Sevilla et al., 2021). Cholinergic
- 62 activation also influences intrinsic properties of neurons, which result in membrane potential
- 63 depolarization (Brown and Adams, 1980), increase in firing rate (Benardo and Prince, 1982), and
- 64 modulation of input/output relationships, for example switching from burst to regular firing (Azouz et al.,
- 65 1994).
- 66 In addition to suppressing several potassium currents (Brown and Adams, 1980; Hoffman and Johnston,
- 67 1998; Buchanan et al., 2010; Giessel and Sabatini, 2010), cholinergic stimulation has been linked to the
- activation of a calcium-activated, non-specific cation current, I_{CAN} (Colino and Halliwell, 1993; Egorov et
- 69 al., 2002; Yoshida et al., 2012). I_{CAN} is attributed to current flowing through channels of the transient
- 70 receptor potential (TRP) family (Guinamard et al., 2010; Reboreda et al., 2011). The canonical TRP
- 71 channel, TRPC, has been implicated in cholinergic-mediated persistent firing ((Zhang et al., 2011; Arboit
- et al., 2020), but see (Egorov et al., 2019)). There is indirect evidence, however, of involvement of
- 73 TRPM4 channels in the cholinergic activation of I_{CAN}. TRPM4 channel activation downstream of group I
- 74 metabotropic glutamate receptors in pre-Botzinger cells (Mironov, 2008), implicates the G_{0/11} pathway
- shared by mGluR_{1/5} and mAChR M_{1/3/5}. Although TRPM4 channels are known to be expressed in the
- soma and apical dendrites of CA1 pyramidal dendrites (Riquelme et al., 2021), their known functions in

these neurons are currently limited to a minor role in the afterdepolarization following action potential trains (Lei et al., 2014) and involvement in NMDA-mediated LTP (Menigoz et al., 2016).

Previously, we found that when triangular shaped current ramps intended to emulate the depolarizing input received by a place cell during a place field traversal (Epsztein et al., 2011) were injected at the soma or dendrites of CA1 pyramidal neurons, they elicited fewer spikes on the down-ramp than on the up-ramp (Upchurch et al., 2022). In the current study, we investigated the effect of cholinergic modulation on this firing pattern *in vitro* (slice electrophysiology) and *in silico* (multi-compartmental NEURON model). We found that, at comparable maximum firing rates, cholinergic activation shifts the center of mass of firing to the latter half of the ramp, both for current injection ramps as well as for synaptically-driven depolarizations. Both CCh and sustained depolarization are required to produce the rightward shift in the center of mass of firing along the ramp. This shift is blocked by antagonists specific for TRPM4 channels or by intracellular Ca²⁺ buffering, but not by IP₃ or ryanodine receptor antagonists. The TRPM4 channels have a micromolar half-activation concentration of Ca²⁺ (Nilius et al., 2004), which implies that a restricted Ca²⁺ nanodomain near the channel mouth is required to elicit substantial opening of TRPM4 channels. Thus, whatever the Ca²⁺ source that activates the TRPM4 channels, it is likely co-localized with them.

Results

Asymmetric firing on symmetric ramps is modulated by cholinergic activation

We have previously used 2 and 10 second long triangular-shaped current ramps (Upchurch et al., 2022) to emulate the depolarizing input received by a place cell during a place field traversal (Epsztein et al., 2011); the amplitude of the ramps was adjusted for each cell to produce peak frequencies between 10 and 25 Hz, as observed in place cells *in vivo* (Hargreaves et al., 2007; Resnik et al., 2012; Bittner et al., 2015). Regardless of whether these ramps are injected at the soma or in the dendrites of CA1 pyramidal neurons, they elicit fewer spikes on the down-ramp than on the up-ramp, due to adaptation mediated by long-term sodium channel inactivation (Fernandez and White, 2010; Venkatesan et al., 2014; Upchurch et al., 2022). Place cell firing is modulated by experience such that the center of mass of the place field shifts in a direction opposite the direction of motion as the environment becomes more familiar (Mehta et al., 2000). This modulation is strongest when animals are first introduced to a novel environment (Roth et al., 2012), suggesting involvement of a novelty signal. Since elevated acetylcholine is thought to be such a signal (Acquas et al., 1996; Giovannini et al., 2001), we investigated the effect of cholinergic neuromodulation on this firing rate adaptation (Figure 1).

Figure 1A1 and 1E1 show typical voltage responses to two-second-long symmetric ramps injected in the soma or dendrites (approximately 200 µm from soma) under control conditions. This type of response

results in a positive value for the normalized difference between spikes fired on the up-ramp versus the down-ramp (we call this an adaptation index, see Methods for definition). A positive index means that neurons fire more on the up-ramp than the down-ramp, whereas a negative value indicates the converse. and is therefore a good metric to determine shifts in the center of mass of the firing of CA1 pyramidal neurons in different conditions. In some trials, under control conditions we applied a baseline depolarization prior to the ramp, in order to capture the variability observed in vivo (Harvey et al., 2009; Epsztein et al., 2011). Application of the cholinergic agonist carbachol (CCh, 2 µM) caused a depolarization of 2-6 mV. We compensated for this depolarization by injecting tonic hyperpolarizing current to reestablish the original membrane potential (see also (Losonczy et al., 2008)), as indicated by an offset from the 0 pA current level in the traces of the injected current ramps. The amplitude of background fluctuations in the resting membrane potential increased from a few tenths of a mV in control to 2-4 mV in CCh. Moreover, the threshold for action potential generation became more hyperpolarized. For all these reasons, we were not able to consistently vary the membrane potential using baseline depolarizations in the presence of CCh, because baseline depolarization alone frequently evoked spiking. As a result of the increased excitability in CCh, smaller current ramps were sufficient to produce the same peak frequencies as in control (note the difference in the injected ramp currents below the voltage trace in Figures 1A1 vs. 1B1 and 1E1 vs. 1F1). Under these conditions, CCh caused a shift of the center of mass of firing to later in the ramp (Figure 1B1 and 1F1), which resulted in a decreased value of the adaptation index which became negative for most cells, as shown in the scatter plot of group data (Figure 1D and 1H). The shift is evident in the plots of the frequency as a function of time (compare Figure 1A2 vs. 1B2 and 1E2 vs. 1F2). As in (Mainen and Sejnowski, 1995), the raster plots of the spike times were characterized by variability in the timing of action potentials among different trials in the same neuron (Figures 1A3, 1B3 and 1E3, 1F3). However, the variability appears to be independent of the amount of current injected, as demonstrated by trials that are grouped as a function of the injected peak current amplitude. Moreover, the raster plots show how the center of mass of firing overall shifted from early in the ramp in control conditions to later in the ramp in the presence of carbachol. This shift was significant for short (2 s) ramps in the soma (control 0.33 \pm 0.02, CCh -0.25 \pm 0.03; t(20) = 16.741; p < 0.0005; n = 21), long (10 s) ramps in the soma (control 0.24 \pm 0.02, CCh -0.33 \pm 0.06; t(18) = 9.854; p < 0.0005; n = 19), as well as for short and long ramps in the dendrites (2 s ramps: control 0.49 ± 0.04 , CCh -0.45 ± 0.07 ; t(18) = 12.529; p < 0.0005; n = 19; 10 s ramps: control 0.37 ± 0.02 , CCh -0.16 ± 0.06 ; t(9) =10.582; p < 0.0005; n = 10).

111

112

113

114

115

116

117

118

119

120

121

122

123

124

125

126

127

128

129

130

131

132

133

134

135

136

137

138

139

140

141

142

143

144

145

146

Plots of instantaneous frequency versus current injection are shown in Figure 1C1, 1C2, 1G1 and 1G2. These plots provide a way to assess firing rate adaptation or acceleration when the injected current is not a square pulse (Venugopal et al., 2015). In control (Figure 1C1 and 1G1), frequencies were higher on the up-ramp (filled circles) and decreased on the down-ramp (open circles) at similar values of injected current. This hysteretic clockwise motion corresponds to spike rate adaptation, in which the firing rate

decreases at a constant value of injected current. In contrast, in the presence of CCh, the motion was variable; it could be essentially linear as shown in the somatic example in Figure 1C2 or even counter-clockwise as in the dendritic example in Figure 1G2. The frequency/current (f/I) plots in Figure 1 – supplement 1 show the clockwise hysteresis in control and different cases of reversal or removal of adaptation in the presence of CCh for somatic recordings, with panels A and B showing acceleration, and panels C and D showing linearization. A linear motion indicates no hysteresis, although often the neurons fire at lower current injections on the down-ramp (defined as sustained linear in (Venugopal et al., 2015)), whereas counter-clockwise motion corresponds to an acceleration of the firing rate that would be observed during injection of a constant current. Both of these variants correspond to an effective removal of the spike rate adaptation by cholinergic activation. These results also demonstrate that cholinergic activity shifts the center of mass of firing to later times during a symmetric ramp. We speculate that the level of cholinergic modulation could therefore be a source of rapid modification of the timing of place cell firing relative to position in the place field. Our summary results in Figure 1 show that carbachol similarly affects 2 s and 10 s ramps, and we present only the data for the 2 second ramps for subsequent figures.

Since the initial membrane potential and the amount of current injected could potentially affect the center of mass of firing, confounding the effects of cholinergic modulation, we plotted the adaptation index as a function of the initial membrane potential (Figure 1 – figure supplement 2A) and of injected current amplitude (Figure 1 - figure supplement 2B), in control conditions and in the presence of carbachol (2 µM) for each trial for all recorded neurons, both for somatic and dendritic recordings. Likewise, since the input resistance of the neuron could potentially skew the center of mass of firing, we plotted the average adaptation index as a function of the steady-state input resistance in control conditions and in the presence of carbachol for each somatic and dendritic recording (Figure 1 - figure supplement 2C). In all cases, it is apparent that the main factor determining the adaptation index, and therefore whether the center of mass of firing occurs earlier or later in the ramp, is the presence or absence of carbachol rather than initial membrane potential, current injection amplitude, or input resistance.

The later onset of spiking in CCh in the experiments described above may be attributable to the smaller current ramps, but the persistence of spiking without adaptation is striking in comparison to control. The use of smaller ramps to achieve similar firing rates may be justified by analogy with the presynaptic action of ACh to reduce glutamate release (Hasselmo, 2006). Since the current injection protocols described above only account for the effects of cholinergic agonists on the postsynaptic neuron, we examined the effects of carbachol on synaptically-driven membrane potential ramps, where pre- and postsynaptic effects can be probed at the same time. To this end, we stimulated the Schaffer collateral fibers with bipolar electrodes and recorded the responses from the somata of CA1 pyramidal neurons (Figure 2). The electrical stimulation consisted of 30 stimuli for a total duration of ~2 s. The stimulation

pattern was adjusted according to a linear, symmetric ramp as in (Hsu et al., 2018), such that the frequency increased and decreased symmetrically, starting at 6.7 Hz and peaking in the middle of the ramp at 25 Hz, the target peak frequency in the current injection experiments. The intensity of stimulation was adjusted such that neurons would fire in response to 40-65% of the total inputs under control conditions, and was kept constant in control conditions and in the presence of carbachol. In both conditions, firing was more frequent in the middle of the ramp, because of the higher stimulation frequency. However, as in the current injection protocols in Figure 1, some variability was observed in the timing of the spikes across trials, as can be appreciated in the raster plots. In control conditions, the neurons tended to fire more in the first half of the ramp (Figure 2A), whereas in the presence of carbachol they tended to fire more on the second half of the ramp (Figure 2B). The adaptation index was calculated in a similar manner as in Figure 1, as the normalized difference between the number of spikes in the first and the second half of the ramp. On average, the adaptation index decreased from 0.18 ± 0.03 in control to -0.17 ± 0.04 in the presence of carbachol, t(10) = 6.873, p < 0.0005, n = 11 (Figure 2C). This shift was partly due to a decrease in the amplitude of the EPSPs (Figure 2D); the average amplitude of the first EPSP in control (8.83 ± 0.82 mV) was significantly larger than the average first EPSP in CCh $(6.81 \pm 0.52 \text{ mV}; t(10) = 4.127; p = 0.002; n = 11)$. In addition, the decay of the EPSPs appeared to slow down later in the ramp in the presence of CCh (compare EPSPs indicated by diamonds in the two conditions), resulting in an increase in temporal summation and excitability. These results show that carbachol tends to shift the center of mass of firing to later in the ramp in the case of a synapticallydriven depolarization as well as in response to a ramp of injected current.

182

183

184

185

186

187

188

189

190

191

192

193

194

195

196

197

198

199

200

201

202

203

204

205

206

207

208

209

210

211

212

213

214

215

216

217

Carbachol is often used to more easily study cholinergic signaling in biological tissues, because it is not susceptible to hydrolysis by acetylcholinesterase, which is preserved and active in hippocampal slices (Avignone and Cherubini, 1999). To verify that the effects of the endogenous neuromodulator were comparable to those of its synthetic analog, we repeated the experiments in Figure 1 with different concentrations of acetylcholine. In this and all following sets of experiments, the amplitude of current injection was adjusted for each cell and condition to produce peak frequencies between 10 and 25 Hz as described above. Acetylcholine caused a depolarization of the V_m in a dose-dependent manner. As before, we compensated for this depolarization by injecting hyperpolarizing current to restore the initial V_m (Figure 3). Like carbachol, acetylcholine shifted the center of mass of firing to later in the ramp, albeit to a more moderate degree (Figure 3A-D). A one-way repeated measures ANOVA was carried out to determine if there was an effect on the adaptation index of three concentrations of ACh within the same neurons. The assumption of sphericity was violated, so a Greenhouse-Geisser correction was applied (ε = 0.574). There was a significant effect of ACh on the adaptation index, plotted in Figure 3E (control 0.35) \pm 0.04; 2 μ M ACh 0.14 \pm 0.04; 10 μ M ACh 0.00 \pm 0.06; 15 μ M ACh -0.02 \pm 0.06; F(1.722, 20.665) = 44.360; p < 0.0005, n = 13). Bonferroni-adjusted post hoc tests demonstrated significant differences between the control condition and all concentrations of ACh (all comparisons p < 0.0005), and between

the lowest concentration and the subsequent higher concentrations (for 2 μ M compared to 10 μ M, p = 0.001; for 2 μ M compared to 15 μ M, p = 0.01). There was not a significant difference between 10 μ M and 15 μ M ACh. Due to likely degradation via acetylcholinesterase, we speculate that the actual concentration in the slices is lower than the applied one. CCh is not susceptible to degradation by acetylcholinesterase, and its concentration, which in our experiments is markedly lower than that used in many studies on cholinergic modulation of neuronal activity (Bland et al., 1988; Fisahn et al., 1998; Knauer et al., 2013), is therefore more consistent, which may explain the more pronounced shift in spiking in Figure 1 as compared to Figure 3. Nonetheless, our results with ACh suggest that there are concentration-dependent effects of the endogenous neuromodulator on firing rate adaptation. Fluctuations in ACh levels could therefore have implications for the firing of a place cell within its place field.

218

219

220

221

222

223

224

225

226

227

228

229

230

231

232

233

234

235

236

237

238

239

240

241

242

243

244

245

246

247

248

249

250

251

252

Cholinergic-associated shift in the timing of firing during the ramp is mediated by TRPM4 channels

An increase in firing on the down-ramp compared to the up-ramp induced by cholinergic activation could result from 1) a decrease in an outward current and/or 2) an increase in an inward current. The cascade of events that follow cholinergic activation in these neurons includes the suppression of a number of outward currents (Halliwell and Adams, 1982; Hoffman and Johnston, 1998; Buchanan et al., 2010; Giessel and Sabatini, 2010), some of which are also involved in firing rate adaptation (Stocker et al., 1999; Gu et al., 2005; Pedarzani et al., 2005; Otto et al., 2006; Chen et al., 2014). Although the SK channel clearly contributes to adaptation when the dendrites are stimulated at high frequency (>50 Hz) (Combe et al., 2018), we have previously examined the contribution of small-conductance calciumactivated potassium (SK) current, M-type potassium current, and A-type potassium current with respect to the asymmetric firing in response to symmetric current ramps (Upchurch et al., 2022). We found that, in the relatively low range of firing frequencies evoked by this type of stimulation, the adaptation induced by these K⁺ currents (including SK) does not play a role in shifting action potentials to earlier times during the ramp. However, cholinergic activation has also been shown to activate a non-specific inward cationic current, I_{CAN}, that is thought to be carried by certain TRP channels (Guinamard et al., 2010; Reboreda et al., 2011). Flufenamic acid (FFA) has been shown to block a variety of TRP channels in hippocampal neurons (Partridge and Valenzuela, 2000) and elsewhere (Guinamard et al., 2013). After observing the typical response to CCh, responses to symmetric ramps were recorded while FFA (100 µM) was applied along with CCh (Figure 4A and 4B). FFA shifted most action potentials back to the up-ramp as shown in the examples in Figure 4A1-4A3 and 4B1-4B3, effectively reversing the shift triggered by CCh. The differences in adaptation index across the three conditions were found to be significantly different by repeated measures ANOVA in both somatic recordings (control 0.35 ± 0.05, CCh -0.36 ± 0.09, CCh+FFA 0.25 ± 0.06 ; F(2,16) = 65.835; p < 0.0005; n = 9; Figure 4A4) and dendritic recordings (control 0.52 ± 0.02, CCh -0.54 \pm 0.11, CCh+FFA 0.20 \pm 0.08; F(2,16) = 60.680; p < 0.0005; n = 9; Figure 4B4). Bonferroni-adjusted pairwise comparisons indicated that for somatic recordings, the differences were significantly different between control and CCh (p < 0.0005), and between CCh and CCh+FFA (p < 0.0005), but not between control and CCh+FFA (p = 0.43). For dendritic recordings, the differences were significantly different between control and CCh (p < 0.0005), CCh and CCh+FFA (p < 0.0005), and control and CCh+FFA (p = 0.02). In most cases, the adaptation index reverted to a positive value with the application of FFA from a negative value in CCh alone, and in all cases was closer to the control value with FFA than with CCh alone. The failure of the adaptation index to return to control values in FFA may reflect an incomplete block of TRP channels or an additional effect of CCh. Overall, these data suggest that the shift in the center of mass of firing to later along the ramp that is associated with cholinergic activity is due, in large part, to activation of TRP channels.

The TRPC subfamily has been implicated as being responsible for I_{CAN} in some neurons and is thought to be activated by elements downstream of muscarinic acetylcholine receptor activation (Putney, 2005), which makes it an attractive candidate, mechanistically, for this cholinergic-mediated shift in action potential firing along the depolarizing ramp. Cholinergic stimulation of G_{q/11}-coupled mAChRs results in phospholipase C hydrolysis of membrane constituent phosphatidylinositol 4,5-bisphosphate (PIP₂) into inositol 1,4,5-trisphosphate (IP₃) and diacylglycerol (DAG). IP₃ stimulates IP₃ receptor (IP₃R) associated Ca²⁺ release from the endoplasmic reticulum, regulating TRPC channel activity via calmodulin (Zhu, 2005), while DAG activates TRPC channels directly (Hofmann et al., 1999; Mederos Y Schnitzler et al., 2018).

In a set of experiments similar to those above, the TRPC-specific antagonist SKF96365 (50 μ M) was added after CCh was applied (Figure 4C and 4D). The differences in adaptation index across the three conditions were found to be significantly different by repeated measures ANOVA in somatic recordings (control 0.43 \pm 0.07, CCh -0.36 \pm 0.09, CCh+SKF -0.24 \pm 0.10; F(2,14) = 42.453; p < 0.0005; n = 8; Figure 4C4) and dendritic recordings (control 0.47 \pm 0.11, CCh -0.24 \pm 0.07, CCh+SKF -0.23 \pm 0.06; F(2,14) = 118.541; p < 0.0005; n = 8; Figure 4D4). However, Bonferroni-adjusted pairwise comparisons demonstrated that the significant differences lie both between control and CCh (soma p < 0.0005; dendrite p < 0.0005) and control and CCh+SKF (soma p = 0.001; dendrite p < 0.0005), not between CCh and CCh+SKF (soma p = 0.68; dendrite p = 1.00). Thus, SKF96365 did not significantly shift the adaptation index in the same manner as did FFA, suggesting that the TRP channels involved in the CCh-mediated forward shift are not of the TRPC subtype.

TRPM4 channels have likewise been implicated in downstream effects associated with G_q-coupled signaling (Launay et al., 2002; Dutta Banik et al., 2018). TRPM4 channels are activated by Ca²⁺ binding to the cytoplasmic side combined with depolarization (Nilius et al., 2003; Autzen et al., 2018), but these channels are impermeable to Ca²⁺. Instead, TRPM4 channels facilitate a rise in [Ca²⁺]_i indirectly, by

depolarizing the membrane potential (Launay et al., 2002) and therefore activating voltage-gated Ca2+ channels (Li et al., 2021). Cationic current through these channels and the resulting [Ca²⁺]_i elevation has been implicated in bursting, persistent firing, and oscillatory activity in some neurons (Lin et al., 2017; O'Malley et al., 2020; Li et al., 2021). In order to investigate the involvement of TRPM4 channels in the cholinergic-mediated shift in adaptation index, the TRPM4 channel antagonist CBA (50 µM) was added after recording the response to CCh (Figure 5A and 5B). Repeated measures ANOVA showed significant differences in the adaptation indices in somatic recordings (control 0.29 ± 0.05, CCh -0.37 ± 0.10, CCh+CBA 0.17 ± 0.07 ; F(2,16) = 66.257; p < 0.0005; n = 9; Figure 5A4) and dendritic recordings (control 0.39 ± 0.07 , CCh -0.41 ± 0.10 , CCh+CBA 0.08 ± 0.05 ; F(2.16) = 34.848; p < 0.0005; n = 9; Figure 5B4). Bonferroni-corrected pairwise comparisons indicated that for somatic recordings, the differences were significant between control and CCh (p < 0.0005), and between CCh and CCh+CBA (p < 0.0005), but not between control and CCh+CBA (p = 0.16). For dendritic recordings, Bonferroni-corrected pairwise comparisons showed that the differences were significant between control and CCh (p < 0.0005), between CCh and CCh+CBA (p = 0.002), and between control and CCh+CBA (p = 0.02). In most cells, the adaptation index became negative in CCh and reverted to a positive value with the addition of CBA, and in all cases the adaptation index was higher in CCh+CBA than in CCh alone.

In order to corroborate that the effect of CBA is due to block of TRPM4 channels, we investigated the effect of a second TRPM4 channel antagonist, 9-phenanthrol, added to CCh in somatic recordings. Figure 5C illustrates the shift of most of the spiking activity towards the up-ramp, moving the adaptation index in the positive direction, when 9-phenanthrol (100 μ M) was applied on top of CCh. The differences in adaptation index between groups are significant, as demonstrated by repeated measures ANOVA (control 0.40 \pm 0.03, CCh -0.14 \pm 0.06, CCh+9Ph 0.19 \pm 0.06; F(2,14) = 57.640; p < 0.0005; n = 8; Figure 5C4). Bonferroni-corrected pairwise comparisons indicated that the differences were significant between control and CCh (p < 0.0005), between CCh and CCh+9Ph (p = 0.001), and between control and CCh+9Ph (p = 0.03).

Taken together, these data with the non-selective TRP channel blocker FFA, the TRPC channel blocker SKF96365, and two different TRPM4 channel antagonists suggest that the shift in adaptation index that we see with CCh is largely mediated through activation of TRPM4, rather than TRPC, channels.

Does Ca²⁺ release from internal sources activate TRPM4 channels?

We next tried to determine the source of Ca^{2+} required to activate TRPM4 channels. We first focused on IP₃ receptors (IP₃Rs), which are activated through mAChRs and G_q as described above, using the antagonist Xestospongin C (Gafni et al., 1997) in the intracellular solution (Figure 6A). Since the antagonists rapidly dialyzed into the cytosol, in this figure control data reflect the effect of the antagonists

before the addition of CCh. We initially used Xestospongin C at 1 µM, which was previously found to be effective in inhibiting TRPM4 channel activation via mGluRs in neurons of the preBötzinger nucleus (Pace et al., 2007). Since this concentration was not effective in preventing the cholinergic shift in the center of mass of firing in our experiments, in six out of nine experiments we increased the concentration to 2 µM. Neither concentration of intracellular Xestospongin C appeared to change the firing features in control conditions. The shift induced by carbachol did not appear to depend on the concentration of Xestospongin C (Figure 6A3), therefore we averaged the data in these two conditions. The adaptation index still decreased significantly (t(8) = 10.574, p < 0.0005; n = 9, as per a paired t-test) from 0.31 ± 0.02 in control conditions to -0.38 ± 0.07 in the presence of CCh (2 µM). This result argues strongly against the hypothesis that the effects of the activation of muscarinic receptors on the shift of the center of mass of firing are mediated by activation of IP₃Rs. Ryanodine receptors (RyRs) are also expressed on the endoplasmic reticulum in CA1 pyramidal neurons, and appear to contribute selectively to spine Ca2+ elevations during LTP at the CA3-CA1 synapses (Raymond and Redman, 2006). We therefore tested the hypothesis that the increase of [Ca²⁺] in a nanodomain leading to TRPM4 channel activation could be due to Ca²⁺-induced Ca²⁺ release (CICR) through RyRs following Ca²⁺ influx through voltage-dependent Ca²⁺ channels. In these experiments, we included ryanodine at 40 μM, a concentration known to inhibit RyRs (Ehrlich et al., 1994; Isokawa and Alger, 2006), in the intracellular solution. Notably, one out of nine of the neurons recorded from in these conditions had a slightly negative adaptation index already under control conditions (Figure 6B3) when RyR were inhibited. Moreover, three more neurons appeared to fire irregularly, with some doublets, under control conditions (an example is shown in Figure 6C), a feature that was not observed in other experimental conditions. This change could be due to the close juxtaposition of RyRs in the endoplasmic reticulum and various K⁺ channels on the membrane of CA1 neurons (Vierra et al., 2019; Tedoldi et al., 2020; Sahu and Turner, 2021). Upon addition of CCh in the bath, the adaptation index became significantly more negative in all nine neurons recorded with intracellular ryanodine, as per a paired t-test (control 0.28 ± 0.05, CCh -0.46 ± 0.07; t(8) = 11.99; p < 0.0005; n = 9), suggesting that RyRs also do not play a role in the cholinergic shift of the center of mass of firing.

322

323

324

325

326

327

328

329

330

331

332

333

334

335

336

337338

339

340

341

342

343

344

345

346

347

348

349

350

351

352

353

354

355

356

Multicompartmental modeling of cholinergic modulation of asymmetric firing responses

We next turned to our detailed multicompartmental model, in order to help identify the underlying mechanisms that contribute to the cholinergic modulation that we observe experimentally *in vitro*. The model was implemented in a reconstructed morphology (Megías et al., 2001) with 144 compartments, each of which can be represented with an equivalent circuit with heterogeneous channel conductance densities and kinetics as described in the Methods. Previously (Upchurch et al., 2022), this model was used to capture the firing rate adaptation observed under control conditions as shown in Figure 7A1 for

short triangular ramps of injected current. The model performs a material balance on Ca²⁺ ions to provide estimated free Ca2+ concentrations in concentric shells beneath the membrane, as shown in the top panels of Figure 7. The control simulation for a 2 second somatic ramp in Figure 7A1 captures the experimentally observed decrease in spike number and frequency on the down-ramp as compared to the up-ramp (adaptation index = 0.28), as well as a slight decrease in spike amplitude, previously shown to be due to a decrease in available Na_V channels (Upchurch et al., 2022). The plot of instantaneous frequency versus level of injected current at the right captures the clockwise pattern observed in Figure 1C1 and G1 corresponding to firing rate adaptation. Figure 7A2 shows the [Ca²⁺] in the outer shell of the soma in nM, Figure 7A3 replots this same concentration in µM (the nanodomain in this case is contiguous with the outer shell so it is not actually a nanodomain), and Figure 7A4 shows that this concentration is insufficient to activate TRPM4 channels. In order to model the effect of CCh, we added a nanodomain for the spatially restricted Ca²⁺ concentration which we hypothesize is sensed by the Ca²⁺ binding site on TRPM4 channels; also note that, as in the experiments, the amount of injected current is lower for the simulated CCh. We showed in Figure 6 that TRPM4 channel activation is not affected by antagonists of IP₃Rs and RyRs, excluding a contribution of Ca²⁺ release from the ER. Although the source of the Ca2+ increase that activates TRPM4 channels is currently unknown, it likely depends in some way upon the activation of voltage-gated Ca²⁺ channels during the ramp. We therefore made the Ca²⁺ influx in the nanodomain proportional to the total instantaneous Ca²⁺ current across the membrane in the model, but only during simulated activation of the muscarinic receptor. Adding the Ca²⁺ influx from an unknown source to a nanodomain in order to simulate bath application of CCh (Figure 7B1) replicates the experimentally observed shift in adaptation index, with more spikes occurring on the down-ramp as compared to the up-ramp (adaptation index = -0.29). The plot of instantaneous frequency versus injected current captures the more extreme observed effect of CCh as illustrated in Figure 1G2; the motion is counter-clockwise corresponding to the acceleration of the firing rate. Figure 7B2 shows the Ca2+ concentration in the outer shell of the soma in nM, Figure 7B3 shows the Ca2+ concentration in µM in the hypothesized nanodomain, and Figure 7B4 shows that this concentration is sufficient to activate TRPM4 channels.

357358

359

360

361

362

363

364

365

366

367

368369

370

371

372

373

374375

376

377

378

379

380

381 382

383

384

385

386

387

388

389

390

391

392

Figure 8 shows why spike rate adaptation is not observed in the simulated presence of CCh. Figure 8A repeats the voltage and current traces from the previous figure, except that the simulated CCh traces (magenta) are superimposed over the control traces (black). Our model includes a four state Markov model of the Na_V channel (see Methods). Occupancy in the open state between action potentials is the substrate for the persistent Na_V current during the interspike interval. Figure 8B shows that the occupancy in the open state of the Markov model of the Na_V channel in the soma is not greatly different between the two conditions, except for excursions produced by spiking, and Figure 8D shows the same result for the somatic Na_V current. Our previous work (Upchurch et al., 2022) attributed spike rate adaptation to reduced persistent Na_V current due to increased long-term inactivation. Figure 8C shows

that although long-term inactivation of the Na_V channel (occupancy in the I2 state) starts later in simulated CCh, it eventually progresses to higher levels than in control because of the increased number of spikes. Nonetheless, no spike rate adaption was observed in simulated CCh in Figure 7B1 because the TRPM4 current is about 4-fold larger than the persistent Na_V current (compare Figures 8D and 8E). Figure 8F shows that the additional TRPM4 current more than compensates for the smaller level of injected ramp current; as a consequence, the net inward current is comparable on the up-ramp and larger in magnitude during the down-ramp for the simulated CCh case than control. This causes spiking to persist longer despite higher levels of Na_V channel inactivation.

When activated by Ca²⁺, TRPM4 channels cause a depolarization and additional spiking that further increases Ca²⁺ influx resulting in a positive feedback loop, with the regenerative inward TRPM4 current contributing to action potential initiation. Figure 9 elaborates on the mechanisms by which Ca²⁺ and voltage differentially contribute to TRPM4 channel activation in removing or reversing spike frequency adaptation. It repeats the traces in control (black) and simulated CCh (magenta) from Figure 7 on an expanded scale and adds two conditions as described below. The insets to the right in Figure 9A show f/l curves that capture the qualitative features of the f/l curves shown in Figure 1C1, C2, G1 and G2. Qualitatively, in control (black traces), there are more spikes on the up-ramp than on the down-ramp, and the instantaneous frequency is lower on the down-ramp for similar values of injected current during the up- ramp. The contribution of the increase in Ca²⁺ concentration in the nanodomain was examined by turning off the voltage-dependence of the TRPM4 channel (light blue traces). In this case, the voltage component of TRPM4 channel activation was set to its steady state value at the resting V_m (see Methods).

Simply adding the nanodomain accomplishes the shift in center of mass (compare blue trace in Figure 9A to control trace in black) and removes the adaptation, with a very slight tendency to accelerate the firing. However, without the contribution of the voltage-dependence of TRPM4 channels, the resulting Ca²⁺ influx is lower than in the original simulation of the effects of CCh (compare the blue traces to the magenta traces in Figure 9B and C), resulting in less TRPM4 channel activation (compare the blue trace to the magenta trace in Figure 9D) and therefore fewer total spikes. To determine the contribution of the positive feedback loop by which Ca²⁺ entry recruits more Ca²⁺ entry via additional spiking and depolarization, we recorded the Ca²⁺ traces in each nanodomain (one for each segment of every section in NEURON, see Methods) of the original CCh simulation (magenta trace in Figure 9C). We then used this Ca²⁺ trace as the [Ca²⁺] in the nanodomain during simulations with the voltage dependence removed as described above. The purple trace in Figure 9A shows that the positive feedback loop added two spikes (16 in the purple trace versus 14 in the blue trace) by slightly increasing the frequency during the spike train and allowing spiking to continue longer. The f/I plot shows a little more acceleration of the firing rate. The purple trace in Figure 9B shows that [Ca²⁺] in the outermost shell is slightly different than

both the blue and magenta traces, reflecting the different numbers of spikes. Note that the purple and magenta traces in Figure 9C are identical because the magenta trace for [Ca²+] in the nanodomain (original CCh simulation) was input to the nanodomain in the simulations shown in purple in the other panels. The additional TRPM4 channel activation (compare purple to blue trace in Figure 9D) results from the increased [Ca²+] in the nanodomain. Adding the full voltage-dependence to the TRPM4 channel slightly raises the overall level of TRPM4 channel activation. The voltage-dependence also allows for fast excursions in channel activation that could contribute to action potential initiation (compare magenta trace in Figure 9D to the blue and purple ones). The voltage-dependence contributes one additional spike (17 in the magenta trace versus 16 in the purple trace in Figure 9A) and accentuates spike rate acceleration due to the positive feedback loop, as shown in the f/l curves.

428

429 430

431 432

433

434

435

436

437

438 439

440 441

442

443

444

445

446

447

448

449

450

451

452

453

454

455

456

457 458

459

460

461 462

463

Evidence for tight coupling between TRPM4 channels and the calcium source that activates them

In order to test experimentally the model prediction that the highly localized Ca2+ elevation in a nanodomain next to the TRPM4 channels gives rise to the CCh-mediated shift in the center of mass of firing, the calcium chelator BAPTA was included in the recording pipette, and somatic recordings obtained before and during addition of CCh. In Figure 10, control data reflect the effect of BAPTA before the addition of CCh, rather than control data such as in previous figures, because the dialysis occurred quickly. As in previous sets of experiments, the amount of current injected was chosen in order to achieve a target firing frequency of 10-25 Hz. With intracellular dialysis of BAPTA, the current needed to reach these frequencies was consistently higher in these experiments (compare scale bars of injected current to those in previous figures). In addition, intracellular dialysis with BAPTA tended to shift the firing earlier in the ramp, with fewer spikes on the down-ramp, therefore making the adaptation index closer to 1. In Figure 10A, 10 mM BAPTA was included in the internal solution. As previously noted, the addition of CCh in the bath caused a depolarization that was compensated for by the injecting hyperpolarizing current. Moreover, despite the presence of BAPTA, the adaptation index became significantly smaller in the presence of CCh, as per a paired t-test (control 0.82 ± 0.05 , CCh -0.12 ± 0.11 ; t(9) = 8.594; p < 0.0005; n = 10; Figure 10A3); therefore, 10 mM BAPTA did not prevent the cholinergic-mediated shift. It has been shown that a higher concentration of BAPTA may be required to prevent TRPM4 channel activation in neurons of the preBötzinger nucleus (Pace et al., 2007; Picardo et al., 2019), therefore, in Figure 10B, BAPTA in the internal solution was increased to 30 mM. With a free [Ca²⁺]_i of 100 nM (see Methods), CCh never produced negative adaptation indices that were seen in previous figures, although the V_m did depolarize and was restored by the injection of tonic hyperpolarizing current. CCh still had a significant effect on the adaptation index, as per a paired t-test (control 0.62 \pm 0.05, CCh 0.37 \pm 0.06; t(7) = 5.069; p = 0.001; n = 8; Figure 10B3). However, when the free $[Ca^{2+}]_i$ was adjusted to 10 nM in the presence of intracellular 30 mM BAPTA (Figure 10C), the adaptation index did not change significantly when CCh was applied in the bath (control 0.73 ± 0.03 , CCh 0.76 ± 0.03 ; t(11) = 0.776; p = 0.45; n = 12;

Figure 10C3). In addition, the depolarization normally observed in the presence of CCh did not occur in these conditions, and the amount of injected current was comparable to that injected in control. These data demonstrate that a concentration of BAPTA higher than the typical value (10 mM) used to disrupt Ca²⁺-dependent mechanisms (Harney et al., 2006) is required to prevent TRPM4 channel activation, and that free [Ca²⁺]_I of <100 nM is necessary to disrupt TRPM4 channel activation. Together, these data suggest a close physical relationship between the source of Ca²⁺ and TRPM4 channels.

470

471

472

464

465

466

467

468

469

Discussion

- Summary of major results
- Whereas place cell firing can only be observed *in vivo*, our bidirectional approach of modeling place cell firing *in vitro* and *in silico* can be precisely targeted to uncover molecular mechanisms responsible for modulation of firing patterns that lead to place cell firing *in vivo*. Manipulations that are difficult or
- impossible even in the *in vitro* preparation can be carried out *in silico* using our detailed multicompartmental model, with the added benefit that the model is transparent. All underlying state
- 478 variables (ion concentrations, channel open fractions) are accessible so that mechanisms can be
- positively identified, facilitating design of experiments to test the putative mechanisms.
- In this study we show that: 1) muscarinic receptor activation shifts the center of mass of firing from earlier
- to later during a depolarizing ramp, through 2) activation of I_{CAN} mediated by TRP channels, most likely of
- the TRPM4 subtype; 3) the shift is not affected by the inhibition of either IP₃Rs or RyRs, arguing against
- 483 a role of Ca²⁺ released from the endoplasmic reticulum in this process; 4) multicompartmental modeling
- suggests a close physical relationship between the source of Ca²⁺ increase and the TRPM4 channels; 5)
- the model prediction is supported by recordings showing that a very high concentration of BAPTA (30
- 486 mM), combined with buffering [Ca²⁺]_i at 10 nM are required to prevent the cholinergic-mediated rightward
- 487 shift.
- 488 More broadly, our results suggest that some rapid changes to place cell firing could be triggered via
- 489 neuromodulation of intrinsic excitability, in addition to and distinct from longer lasting experience-
- 490 dependent changes that are brought about by synaptic and structural plasticity. Specifically, we
- 491 speculate that increasing levels of ACh could lead to forward shifts in place cell firing, whereas
- 492 decreasing levels of ACh could contribute to backwards shifts.

493

494

Mystery current identified

Muscarinic activation of a Ca²⁺-dependent nonselective cation current in rat CA1 pyramidal neurons has been known for nearly three decades (Colino and Halliwell, 1993; Fraser and MacVicar, 1996; Dasari et al., 2017). A previous study (Yamada-Hanff and Bean, 2013) found that in mouse CA1 neurons as well, muscarinic stimulation not only inhibits background potassium currents but also activates a nonselective cation current. They found that the latter effect was dominant and in fact converted CA1 pyramidal neurons into pacemakers with the application of 5-25 μM acetylcholine, 5-25 μM carbachol, or 5-10 μM oxotremorine-M. They suggested TRPC channels might mediate this current but were unable to positively identify the source of the nonselective cation current. Based on our results, this unidentified channel could be the TRPM4 channel. We show that TRPM4 channels primarily mediate a nonspecific Ca²⁺-activated cation current evoked by cholinergic modulation in CA1 pyramidal neurons. Our model shows that the activation of TRPM4 channels contribute an additional inward current that activates and deactivates slowly upon depolarization. In the case of synaptically-driven depolarizations (Figure 2), this inward current, with its slow kinetics (see Figures 8 and 9) is likely to cause an increased decay time of the EPSPs (see Figure 2). This aspect has likely implications for synaptic integration by these neurons, as shown by the observation of an impairment of LTP in TRPM4 knockout mice (Menigoz et al., 2016).

One of our most surprising findings was that TRPC channels did not seem to play a role in cholinergic modulation of the firing pattern along a triangular ramp. TRPC channels have been implicated in cholinergic signaling via direct activation by DAG, one of the two bioactive molecules generated by PLC hydrolysis of PIP₂ (the other being IP₃). Cholinergic-associated persistent firing, whereby neurons continue to fire after a depolarizing stimulus has ceased, has been attributed to activation of TRPC channels (Zhang et al., 2011; Arboit et al., 2020). However, the presence of cholinergic-induced persistent firing in TRPC knockout mice has called this into question (Egorov et al., 2019). In a recent study, TRPM4 channels were found to be involved in persistent firing generated upon Ca²⁺ influx via T-type channels in thalamic neurons (O'Malley et al., 2020). Delayed bursting in a subtype of cerebellar granular cells was also shown to be mediated by TRPM4 channels (Masoli et al., 2020). Our study therefore provides further evidence regarding the role of these channels in the control of neuronal firing, possibly including persistent firing.

Nanodomain resulting from colocalization of cholinergic-induced increases in [Ca²⁺]_i and TRPM4 channels

In HEK cells transfected with cDNA encoding TRPM4 channels, and in cardiac myocytes, activation of TRPM4 channels is secondary to IP₃ receptor activation (Launay et al., 2002; Gonzales et al., 2010; Gonzales and Earley, 2012), suggesting that TRPM4 channels in myocytes are activated by Ca²⁺ release from intracellular stores. Furthermore, in situ proximity ligation assay was used to demonstrate colocalization of TRPM4 channels and IP₃Rs in human detrusor smooth muscle cells (Provence et al.,

2017). In addition, in neurons of the preBötzinger nucleus TRPM4 channels are recruited by metabotropic glutamate receptors to generate robust inspiratory drive potentials through IP $_3$ R activation (Pace et al., 2007). Surprisingly, we found that Ca $^{2+}$ release from the ER was not involved in the cholinergic shift of the center of mass of firing, since neither the IP $_3$ R antagonist Xestospongin C (1-2 μ M) nor the RyR antagonist ryanodine (40 μ M) prevented the effects of carbachol. Therefore, although the mechanisms that produce the micromolar [Ca $^{2+}$] increases needed for TRPM4 channel activation are unknown, our results point to these channels acting as coincidence detector, requiring both muscarinic receptor activation and depolarization-induced Ca $^{2+}$ influx during the ramp to be activated

Our modeling results imply that, upon activation of muscarinic receptors, TRPM4 channels have privileged access to a nanodomain in order to achieve the micromolar concentrations of Ca²⁺ necessary for their activation (Nilius et al., 2004), since microdomains (like the multicompartmental model's outer shell) only achieve submicromolar concentrations (Fakler and Adelman, 2008). The affinity of TRPM4 channels for Ca²⁺ is heavily dependent on the availability of PIP₂ (Nilius et al., 2006) and binding of ATP and calmodulin or PKC-dependent phosphorylation (Nilius et al., 2005), which all function to increase the sensitivity of TRPM4 channels for Ca²⁺. If under our conditions, the dependence of TRPM4 channels on [Ca²⁺] has a much lower EC₅₀ and/or is much steeper than in the model we implemented (Nilius et al., 2004), perhaps the nanomolar [Ca²⁺] in the outer shell could be sufficient to activate TRPM4 channels. However, the experimental result that 30 mM BAPTA was required to block the TRPM4 channels' access to Ca²⁺ argues for a spatially restricted nanodomain. In a previous study, we found that intracellular BAPTA at a concentration 5 mM can mimic SK block (Combe et al., 2018), presumably by interfering with the calcium activation of those channels. The requirement of using 30 mM BAPTA while buffering free [Ca²⁺]_i to 10 nM in order to prevent TRPM4 channel activation suggests that TRPM4 channels are activated by a more spatially restricted Ca²⁺ domain than SK channels.

Convergence of pharmacological blockers

One caveat for our experimental results is that TRP channel blockers, like most drugs, have been reported to have some non-specific effects. In cardiac cells, both CBA and 9-phenanthrol have been shown to decrease the Ito1 potassium current, attributed to Kv4.3 (Veress et al., 2018; Dienes et al., 2021) and a late sodium current (Hou et al., 2018; Dienes et al., 2021). Kv4.3 is likely more important in interneurons than in pyramidal cells in the CA1 area (Martina et al., 1998), and neither of the two currents are affected by FFA at the concentration we used here (Guinamard et al., 2013). The other reported non-specific effects do not overlap between the three blockers, flufenamic acid, CBA and 9-phenanthrol (Simard et al., 2012; Guinamard et al., 2013; Veress et al., 2018; Dienes et al., 2021). The convergent effects of these three distinct drugs implicate TRPM4 channels as the most probable effector of the CCh-mediated modulation of the center of mass of firing. A similar pharmacological approach was

used to implicate TRPM4 channel activation in subthreshold oscillations underlying pacemaker firing of chemosensory neurons in the retrotrapezoid nucleus (Li et al., 2021).

Diverse cholinergic effects on CA1 pyramidal neurons

In CA1 pyramidal neurons, ACh binding to muscarinic receptors results in neuromodulation of neuronal excitability and presynaptic release probability. In our study, focused mainly on intrinsic properties, the predominant effect of ACh and CCh was to activate TRPM4 channels; however, the effect of ACh on CA1 pyramidal cells in vivo is multipronged. Muscarinic receptors are known to suppress several K⁺ currents in CA1 pyramidal neurons (Halliwell and Adams, 1982; Hoffman and Johnston, 1998; Buchanan et al., 2010; Giessel and Sabatini, 2010). The effects of ACh on SK, M-type currents and I_{CAN} are mediated by M₁ (G₀-coupled) receptors (Dasari and Gulledge, 2011). Synaptic depression of Schaffer collateral inputs to CA1 is mediated by M₄ (G_i-coupled) receptors (Dasari and Gulledge, 2011) located on presynaptic glutamatergic terminals, and synaptic depression of temporoammonic pathway glutamatergic inputs to CA1 is mediated by M₃ (G₀-coupled) receptors (Palacios-Filardo et al., 2021). When we used a synaptically-driven depolarization (Figure 2), decreased release from Schaffer collateral was indicated by the smaller amplitude EPSPs in the presence of CCh. In these experiments, as in the current injection protocols, the center of mass of firing occurred earlier in the ramp in control and shifted to later in the ramp in the presence of CCh, suggesting that a combination of pre- and postsynaptic effects of cholinergic agonists can contribute to the shift. Moreover, the cholinergic down-regulation of these afferents justifies the use of smaller depolarizing current injection ramps in our recordings in the presence of carbachol, because less current injection is required to produce the same output frequencies due to enhanced intrinsic excitability in carbachol.

In a model of place field formation (Savelli and Knierim, 2010), if a neuron randomly fires within a place field (Bittner et al., 2015), its inputs from the currently active grid cells are strengthened and the input from those grid cells onto silent cells are weakened. Previously, ACh was thought to act in a manner consistent with volume transmission (Dannenberg et al., 2017). Recently, this view has been challenged by the finding that all hippocampal cholinergic terminals form synapses (Takács et al., 2018), and vesicles dock only at synapses. Since cholinergic neuromodulation of TRPM4 channels greatly increases excitability in CA1 pyramidal cells, selective synaptic ACh inputs may underlie the formation of place fields in a novel environment. Moreover, (Takács et al., 2018) found that the ACh terminals co-released GABA in separate vesicles, and that ACh acting on M₂ (G_i-coupled) autoreceptors on cholinergic terminals inhibited the release of both ACh and GABA. Future work is required to disentangle the distinct effects of ACh acting at the various muscarinic receptors (M₁-M₅).

Acetylcholine, Novelty and Place Field Shifts

Acetylcholine acting at muscarinic receptors has been hypothesized to be a global novelty signal in the dentate gyrus (Gómez-Ocádiz et al., 2022), dorsal hippocampus (Huff et al., 2022), and the parahippocampal gyrus (Frank and Kafkas, 2021). A novel unconditioned stimulus caused a large increase in ACh extracellular levels in the hippocampus, but little locomotion (Acquas et al., 1996). On the other hand, hippocampal ACh release in an animal placed in a novel environment has two components, one related to novelty, that disappears in a familiar environment (Thiel et al., 1998), and one related to motor activity, associated with increased exploration (Giovannini et al., 2001). Indeed, a recent fiber photometric study showed that part of the population activity in medial septal cholinergic neurons is correlated with the logarithm of running speed (Kopsick et al., 2022). We are primarily interested in the component of the ACh signal related to novelty because of previous studies demonstrating modulation of place cell firing that was more pronounced during the first day in a novel environment (Roth et al., 2012).

In vivo recordings in rats demonstrated that place fields expand and the center of mass shifts backward with respect to the direction of travel on continuous tracks over several laps during each recording session (Mehta et al., 2000). This phenomenon was predicted by modeling studies that implemented Hebbian plasticity in the form of NMDA-mediated LTP (Abbott and Blum, 1996; Blum and Abbott, 1996). whereby spatially tuned input gradually strengthens over repeated traversals of a place field, causing a CA1 place cell to fire earlier in the place field. NMDA blockers were subsequently shown to occlude the backwards shift of the place field (Ekstrom et al., 2001) and an NMDA agonist partially restored it in aged rats (Burke et al., 2008). Calcium imaging in mice running on a treadmill in a virtual environment showed an abrupt backward shift in place cell firing (relative to where the first episode of place field firing occurred) during the first exposure to a novel environment (Priestley et al., 2022), as well as much smaller backward shifts in place fields in novel environments that leveled off as the animals became more familiar with the environment during subsequent exposures (Dong et al., 2021). These backwards shifts, which were much larger than those observed previously and attributed to Hebbian plasticity, were ascribed to behavioral time scale plasticity, which is also dependent on NMDA receptor activation, and strengthens glutamatergic inputs active during an asymmetric seconds-long window skewed towards synapses activated before a burst triggered by a dendritic plateau (Bittner et al., 2017).

Despite the ability of elegant theories of synaptic plasticity to account for backward shifts in the center of mass of the place field, forward shifts have also been observed. Forward shifting of the center of mass of place field firing occurred, shifting toward prospective goal locations in the continuous T-maze alternation task as a reward was approached (Lee et al., 2006). Thus, task-specific demands may allow for the modulation of firing fields by neuromodulators such as ACh and dopamine. In a study that did not involve

reward, but only exploration of a novel virtual linear maze (Dong et al., 2021), the center of mass of CA1 place fields in laps 2-4 were forward shifted compared to the first lap, for cells that already had a place field on the first lap (a lap required approximately 25 seconds). Laps 5 and beyond were backward shifted compared to the immediately preceding lap, so averaging over all runs, the place field was shifted backwards. Perhaps the neuromodulatory environment, including cholinergic tone, was different during the first four laps. The data in that study indicated that backward shifting in CA1 in a novel environment is due to a combination of place field expansion, skewness and translation of the point at which peak firing occurs. They suggested that since skewness and width dynamics are inconsistent across studies, multiple mechanisms may be involved in place field shifting.

Ideas and Speculations: Implications of our results for place fields in intact rodents

Our results suggest that increasing levels of ACh could lead to forward shifts in place field center of mass whereas decreasing levels of ACh could contribute to backwards shifts. Since cholinergic activity in CA1 is elevated when animals encounter novel environments, our results with CCh could correspond to an initial encounter with a novel environment, where firing of an existing place cell is shifted "forward" or later during the depolarizing ramp that simulates spatially-tuned input. Our control conditions, then, would be analogous to lower cholinergic tone, occurring as an animal becomes familiar with an environment, and the associated "backward" shift earlier in the depolarizing ramp. The rapid modulation of ion channels by removal of cholinergic tone could therefore provide a possible mechanism for the rapid shifting of place cell firing in a novel versus familiar environment, perhaps complementary to Hebbian plasticity that develops over time.

If our hypothesis is correct, optogenetic silencing of medial septum cholinergic afferents to CA1 during runs through a place field in a novel environment should partially occlude backwards shifts in place field center on subsequent runs that are due to diminished ACh in a familiar environment. Optogenetic stimulation of the same afferents during runs in a familiar environment should induce forward shifts in place field centers. Behaviorally, it could be informative to design experiments to test the effects of these manipulations on the animal's subjective sense of position, for example, demonstrated by overshoot or undershoot locations where the animal has been trained to pause.

There is a growing realization that there may be multiple mechanisms for place field shifting in addition to the well-known mechanisms for backwards shifts dependent on Hebbian plasticity (Blum and Abbott, 1996; Ekstrom et al., 2001; Burke et al., 2008; Roth et al., 2012; Mehta et al., 2000) or, more recently, behavioral timescale synaptic plasticity (Bittner et al., 2017; Priestley et al., 2022). We propose that neuromodulation of intrinsic properties by ACh, and potentially other neuromodulators like dopamine,

provide an additional level of modulatory control in parallel with synaptic plasticity mechanisms, contributing to rapid place field shifts.

Materials and Methods

Key Resources Table						
Reagent type (species) or resource	Designation	Source or reference	Identifiers	Additional information		
Strain, strain background	Male Sprague Dawley rats	Envigo (Inovit)	Hsd:Sprague Dawley® SD®	7-12 weeks old when sacrificed for experiments		
chemical compound, drug	NBQX	Alomone Labs	cat# N-186	AMPA receptor antagonist		
chemical compound, drug	DL-APV	HelloBio	cat# HB0252	NMDA receptor antagonist		
chemical compound, drug	Gabazine	Alomone Labs	cat# G-216	GABA _A receptor antagonist		
chemical compound, drug	CGP55845	Abcam	cat# ab120337	GABA _B receptor antagonist		
chemical compound, drug	Carbachol	Tocris	cat# 2810	Acetylcholine receptor agonist		
chemical compound, drug	Acetylcholine,	Sigma-Aldrich	cat# A6625	Ligand for acetylcholine receptors		
chemical compound, drug	flufenamic acid	Sigma-Aldrich	cat# F9005	TRP channel antagonist		
chemical compound, drug	SKF96365	Alomone Labs	cat# S-175	TRPC channel antagonist		

chemical compound, drug	СВА	Tocris	cat# 6724	TRPM4 channel antagonist
chemical compound, drug	9-phenanthrol	Tocris	cat# 4999	TRPM4 channel antagonist
chemical compound, drug	Xestospongin C	Abcam	cat# ab120914	IP₃R antagonist
chemical compound, drug	low molecular weight heparin	Sigma-Aldrich	cat# H3149	IP₃R antagonist
chemical compound, drug	D-myo-IP ₃	Cayman Chemical	cat# 60960	IP₃R agonist
chemical compound, drug	Adenophostin A	MilliporeSigma	cat# 115500	IP₃R agonist
chemical compound, drug	Ryanodine	HelloBio	cat# HB1320	RyR antagonist at [µM]
chemical compound, drug	Ruthenium red	Tocris	cat# 1439	RyR antagonist
chemical compound, drug	Dantrolene	Tocris	cat# 0507	RyR antagonist
chemical compound, drug	caffeine	Tocris	cat# 2793	RyR agonist
chemical compound, drug	Thapsigargin	Alomone Labs	cat# T-650	SERCA inhibitor
chemical compound, drug	BAPTA tetra- potassium salt (K4- BAPTA)	Sigma-Aldrich	cat# A9801	fast Ca ²⁺ chelator
Software, algorithm	MAXCHELAT OR, WEBMAXC EXTENDED	https://somapp. ucdmc.ucdavis. edu/pharmacol ogy/bers/maxc helator/webma xc/webmaxcE. htm		Online free metal calculator
Software,	SPSS	IBM	RRID:SCR_00	Statistics

algorithm			2865	software
Software, algorithm	NEURON	Hines and Carnevale, 1997; Carnevale and Hines, 2006	doi:10.1162/ne co.1997.9.6.11 79; doi.org/10.101 7/CBO9780511 541612	Computational modelling and simulation software
other	Laerd Statistics	https://statistics .laerd.com/		Online tutorial and software guide

Experimental methods

Slice preparation. All the procedures described below were conducted according to protocols developed by following guidelines on the responsible use of laboratory animals in research from the National Institutes of Health and approved by the Louisiana State University Health Sciences Center-New Orleans Institutional Animal Care and Use Committee (IACUC, internal protocol numbers 3583 and 3851). Animals were housed in pairs, whenever possible; in the event of single housing, Bed-r'nest pucks (Andersons Lab Bedding) were provided for enrichment purposes.

For these experiments, 400 µm-thick slices were prepared from 7 to 11-week-old male Sprague Dawley rats as previously described (Combe et al., 2018). Briefly, rats were deeply anesthetized via intraperitoneal injection of ketamine and xylazine (90 and 10 mg/kg, respectively), until the disappearance of the toe-pinch and palpebral reflexes. After trans-cardiac perfusion with ice-cold solution, decapitation, and rapid removal of the brains, transverse hippocampal slices were cut using a vibratome. Slices were then transferred to a chamber filled with an oxygenated artificial cerebro-spinal fluid (ACSF) containing, in mM: NaCl 125, NaHCO₃ 25, KCl 2.5, NaH₂PO₄ 1.25, MgCl₂ 1, CaCl₂ 2, dextrose 25, ascorbate 1, sodium pyruvate 3.

Patch clamp electrophysiology. After recovery, individual slices were transferred to a submerged recording chamber, and superfused with ACSF at about 2 ml/min; the solution was warmed through an inline heater and measured to keep it at a temperature of 34-36°C in the chamber.

CA1 pyramidal cells were identified via differential interference contrast-infrared video microscopy. Whole-cell current clamp recordings were made using Dagan BVC 700A amplifiers in the active "bridge" mode. Recording pipettes were filled with an internal solution that contained, in mM: potassium methanesulphonate 125, KCl 20, HEPES 10, EGTA 0.5, NaCl 4, Mg₂ATP 4, Tris₂GTP 0.3,

phosphocreatine 14. The electrode resistance was 1-3 M Ω for somatic recordings and 3-5 M Ω for dendritic recordings. Series resistance was monitored throughout the recordings and was usually less than 20 M Ω ; recordings were discarded when series resistance reached 25 M Ω or 30 M Ω , for somatic and dendritic recordings, respectively. Cells with resting membrane potentials depolarized beyond -60 mV at break-in were discarded.

To investigate the contribution of intracellular Ca²⁺ signaling to TRPM4 channel activation and the cholinergic shift in the center of mass of firing, in some sets of experiments, the internal patch clamp solution was modified as follows. In some experiments, EGTA was replaced by higher concentrations (10 or 30 mM) of the faster Ca²⁺ chelator BAPTA tetra-potassium salt. When 30 mM BAPTA was included, 0.69 mM or 5.7 mM Ca²⁺ was added to the internal solution to give 10 or 100 nM free [Ca²⁺], respectively, at 33°C, pH 7.3 and an overall ionic concentration of 300 mM, according to the online program MAXCHELATOR, WEBMAXC EXTENDED version

(https://somapp.ucdmc.ucdavis.edu/pharmacology/

bers/maxchelator/webmaxc/webmaxcE.htm). In other experiments, Xestospongin C (1-2 μ M) or ryanodine (40 μ M) were added to the internal patch clamp solution to block IP₃Rs and RyRs, respectively. Xestospongin C and ryanodine were dissolved in DMSO; in this case the [DMSO] in the final solution was \leq 0.2% due to the limited solubility of these compounds. As in (Pace et al., 2007), Xestospongin C was added to the standard intracellular solution immediately prior to use and discarded after 2 hours. In all these cases, intracellular dialysis appeared to take effect quickly, so the control data refer to the effect of the modified internal solution. Nonetheless, dialysis was allowed for at least 20 minutes in these experiments to make sure that the drug could diffuse into distal compartments.

NBQX (10 μ M), DL-APV (50 μ M), Gabazine (12.5 μ M) and CGP55845 (1 μ M) were applied in the external solution in all experiments, except those in which the Schaffer Collateral fibers were electrically stimulated (Figure 2), to block glutamatergic and GABAergic neurotransmission, respectively, in order to isolate the contribution of the intrinsic ion channels to the ramp responses. Carbachol (2 μ M), acetylcholine (2, 10, or 15 μ M), flufenamic acid (100 μ M), SKF96365 (50 μ M), CBA (50 μ M), and 9-phenanthrol (100 μ M) were added to the external solution as needed, from stock solutions made with water, DMSO, or ethanol; the concentration of ethanol or DMSO in the final solution was \leq 0.1%. Carbachol, 9-phenanthrol, and CBA were purchased from Tocris, CGP55845 and Xestospongin C from Abcam (Cambridge, MA), DL-APV and ryanodine from HelloBio (Princeton, NJ), NBQX, Gabazine, and SKF96365 from Alomone Labs (Jerusalem, Israel), and acetylcholine, flufenamic acid, and K4-BAPTA from Sigma (St. Louis, MO).

In order to approximate the depolarizing input that place cells receive as an animal traverses the place field, ramp-shaped depolarizing current injections were applied via the recording electrode to CA1 pyramidal neurons at either the soma or the apical dendrite (150-250 µm from soma). Two second ramps (1 s up, 1 s down) and ten second ramps (5 s up, 5 s down) were applied to simulate different running

speeds. Current amplitude was adjusted to evoke peak frequencies between 10 and 25 Hz, comparable to place cell firing as recorded *in vivo* (Hargreaves et al., 2007; Resnik et al., 2012; Bittner et al., 2015).

Electrical stimulation was achieved by delivering constant current pulses through a tungsten bipolar electrode placed in the stratum radiatum of area CA1 to stimulate the Schaffer collateral fibers from CA3 pyramidal neurons. The instantaneous input frequency of stimulation was adjusted according to a linear, symmetric ramp (see also (Hsu et al., 2018). The total duration of the ramp was ~2 s and the peak frequency at the center of the ramp was 25 Hz, our target for the maximum peak frequency in the ramp current injections (see above). The intensity of stimulation was adjusted such that neurons would fire in response to 50-70% of the total inputs and kept constant in control conditions and in the presence of carbachol. For each neuron and condition, we averaged the trials where the neurons did not fire in response to the first pulse in the synaptic ramp and the amplitude of the EPSPs was measured to estimate the degree of cholinergic modulation of presynaptic release. Antagonists of synaptic transmitter receptors were omitted in these experiments.

- Experimental design and statistical analyses
- Experimental data were recorded and analyzed with Igor Pro software (WaveMetrics). Left or rightward shifts in firing along the current ramp were quantified as an adaptation index, as previously described (Upchurch et al., 2022):

Positive values indicate firing predominantly on the up-ramp, while negative values indicate firing mostly on the down-ramp. For synaptically driven membrane potential ramps, the adaptation index was calculated in a similar manner, where the up-ramp consisted of the first 15 (out of 30) stimuli. An adaptation index of zero indicates symmetry in the number of action potentials on the up-ramp and the down-ramp. Plots of instantaneous frequency versus time (f/t) or current (f/l) use the time or current value at the midpoint of the interspike interval (ISI), respectively. Current amplitude is relative to tonic baseline current. Raster plots in Figures 1 and 2 show the timing of action potential firing for several trials in control conditions and in the presence of carbachol, where time = 0 indicates the beginning of the ramp. The tick marks represent the timing of each action potential (when the V_m crossed -40 mV).

An n = 6-12 is required for a typical patch clamp electrophysiology experiment that has a difference in means of 1.3-2X and a standard deviation of 0.2-0.3 for p = 0.05 and a power of 0.9 (Cohen, 1977). Each experimental group in this study is made up of n \ge 8 recording sessions; the number of cells recorded for each experiment is indicated in the Results section. Recordings were from one cell per slice; typically, a maximum of three recordings were obtained for each animal. Biological replicates (recording

from different cells) were $n \ge 8$ for each experiment and (recordings from different animals) $n \ge 6$ for each experiment.

Statistical analyses were performed in SPSS (IBM, RRID:SCR_002865), following the tutorials and software guide from Laerd Statistics (2015, https://statistics.laerd.com/). Comparisons were made in the same cell before and during pharmacological treatment; the summary plots for these data include individual points and means ± standard error of the mean. Parametric analyses (paired samples t-test and repeated-measures ANOVA) were used to compare treatments in the same neurons, since data were normally distributed as determined by the Shapiro-Wilk test for normality. Significant differences demonstrated by repeated measures ANOVA were followed up by post-hoc analysis using Bonferronicorrected pair-wise comparisons. Differences were considered to be statistically significant when p < 0.05. Outliers, as assessed by boxplots, were not removed from analysis. To check the effect of the outliers, analyses were also performed after removing outliers, and with non-parametric tests keeping the outliers. The significance did not change, and for consistency, the results of parametric tests are reported with all data included.

777 Data Availability

765

766

767

768

769

770

771

772

773

774

775

776

- 778 Data generated and analyzed during the study are included in the manuscript and supporting files.
- 779 Source data are provided for all experimental figures.
- 780 Computational Modeling

781 A multicompartmental CA1 pyramidal neuron model from our laboratory was used as a starting point 782 (Upchurch et al., 2022). This model was based on the model in the study by (Poirazi et al., 2003a), with 783 subsequent changes made in studies by (Shah et al., 2008), (Bianchi et al., 2012), and (Combe et al., 784 2018). The model (Figure 11A) was created from a reconstructed morphology (Megías et al., 2001) with 785 144 compartments and implemented in the NEURON simulation software package (Hines and 786 Carnevale, 1997; Carnevale and Hines, 2006). The following currents (Figure 11B) were modeled using Ohmic drive and conductances in parallel with a membrane capacitance (C_M): a Na⁺ current (I_{Na}), L-type 787 (I_{CaL}) , R-type (I_{CaR}) , and T-type (I_{CaT}) Ca^{2+} currents, two delayed rectifiers $(I_{Kv1}$ and $I_{Kv2})$, an A-type K^{+} 788 789 current (I_A), an inward rectifying potassium current (I_{KIR}), a nonspecific Ca²⁺-activated current (I_{CAN}), a 790 hyperpolarization-activated mixed cationic h-current (I_h), and a leak current (I_L). All currents were as in 791 the previous model except (I_{CAN}), which was added to the model. In the soma and apical dendrites, we 792 kept the Markov model (Figure 11C) of the Na_V channel that we modified from (Balbi et al., 2017). This 793 Markov model was tuned to replicate the distance-dependent long-term inactivation of Na_V1.6 found in 794 the literature (Mickus et al., 1999) that causes spike frequency adaptation and the difference in half 795 activation between the soma and dendrites supported by (Gasparini and Magee, 2002). The sevenfold 796 gradient in the h-conductance supported by (Magee, 1998), sixfold gradient in A-type potassium channels supported by (Hoffman et al., 1997) and lower sodium conductance in the dendrites versus the soma (75% of somatic value) supported by (Gasparini and Migliore, 2015) were also retained. A spine factor, to account for the additional membrane area due a higher density of spines (Megías et al., 2001) was varied as described in (Upchurch et al., 2022), and a sigmoidal decrease in membrane and axial resistance was implemented to account for the decrease in input resistance along the apical dendrites (Magee, 1998; Poirazi et al., 2003b).

The calcium handling for the model (see top panels in Figure 7A1 and B1) was modified from (Ashhad and Narayanan, 2013). The model performs a Ca^{2+} material balance on four shells in each compartment, and incorporates radial and longitudinal diffusion ($D_{Ca}\nabla^{2}[Ca^{2+}]$), stationary and mobile Ca^{2+} buffers (R. Buf), calcium leak through endoplasmic reticulum leak channels (J_{leak}), Ca^{2+} uptake from a sarcoplasmic/endoplasmic reticulum Ca^{2+} ATPase pump (J_{SERCA}), IP_{3-} mediated Ca^{2+} release (J_{IP3R}), a plasma membrane extrusion pump (J_{Pump}) and Ca^{2+} from voltage gated channels on the membrane (J_{VGCC}). The latter two terms appear only in the outer shell. Details on the implementation of diffusion, the buffers, calcium leak and the pumps are described in (Ashhad and Narayanan, 2013). The differential equation for cytosolic calcium is described below.

$$\frac{\partial [Ca^{2+}]}{\partial t} = D_{Ca} \nabla^2 [Ca^{2+}] + A J_{IP3R} + B (J_{leak} - J_{SERCA}) + R_{Buf} + J_{VGCC} - J_{Pump}$$

We used an equation for Ca²⁺ dynamics in the nanodomain that is agnostic as to the source of the Ca²⁺ contributing to the nanodomain:

$$\frac{d[Ca^{2+}]_{ND}}{dt} = X * I_{Ca} + \frac{[Ca^{2+}]_{outer\ shell} - [Ca^{2+}]_{ND}}{400ms}$$

where X is a scale factor representing the effect of a small volume for Ca^{2+} accumulation in the restricted nanodomain. The model is agnostic regarding the source of the Ca^{2+} entry into the nanodomain, which was arbitrarily set to be proportional to the total Ca^{2+} current I_{Ca} . In the absence of simulated application of CCh, X=0 so that the TRPM4 channel senses the bulk Ca^{2+} concentration in the outer shell. To simulate application of CCh, in contrast with our previous modeling efforts, based on a central role for IP_3R (see Figure 11 – Figure supplement 1), [IP3] and therefore J_{IP3R} was not increased from baseline levels; instead, influx to the nanodomain from an unknown source was simulated by setting X=500. The relatively long time constant reflected the spatially restricted nature of the nanodomain, with some postulated impediment to diffusion between the nanodomain and the bulk cytosol. In one simulation (purple traces in Figure 9), the $[Ca^{2+}]_{ND}$ for every segment in every section was recorded was recorded in

the original CCh simulation (magenta traces) and played back using NEURON's vector play method in the model lacking the voltage-dependence of the TRPM4 channels in order to eliminate differences in $[Ca^{2+}]_{ND}$ between models and focus solely on the contribution of the voltage-dependence unrelated to additional Ca^{2+} influx.

The TRPM4 model was modified from (Nilius et al., 2004) and assumes that the required binding of Ca²⁺ to the channel precedes voltage-dependent channel activation. The model has three different states, an unbound state, a Ca²⁺ bound closed state, and an open state.

$$TRPM4 \Leftrightarrow TRPM4 \ bound \ to \ Ca^{2+} \stackrel{\longleftrightarrow}{\underset{\alpha(V),\beta(V)}{\Longleftrightarrow}} Open \ TRPM4 \ channel$$

 Ca^{2+} binding is assumed to be much faster than the voltage dependent gating and is assumed to instantaneously reach the steady state binding determined by the dissociation constant K_d (87 μ M). The fraction of open channels m relaxes to the steady state activation m_{∞} with a time constant, τ , with first order kinetics:

837
$$\alpha' = \frac{\alpha}{1 + \frac{Kd}{\left[C\alpha^{2}\right]_{ND}}}, m_{\infty} = \frac{\alpha'}{\alpha' + \beta}$$
 $\tau = \frac{1}{\alpha' + \beta}$

where α is the forward rate of Ca²⁺ bound TRPM4 channel opening, $\alpha(V) = 0.0057$ exp(0.0060 V), α' is the forward rate scaled by the fraction of Ca²⁺ bound channels, β is the backward rate of TRPM4 channel closing, $\beta(V) = 0.033$ exp(-0.019 V) and [Ca²⁺]_{ND} is the Ca²⁺ concentration in the nanodomain. When removing the voltage-dependence of TRPM4 channels, we set V in the equations above to the steady-state value at -60 mV. We injected enough current into the model to hold the membrane potential at -60 mV long enough for all transients to equilibrate before injecting a two second temporally symmetric current ramp in the soma. The amplitude of the ramp was adjusted to reach similar peak frequencies as in the experiments, 10 to 25 Hz.

The persistent current during the interspike intervals determines the spike frequency. In order to focus on the rate determining currents in Figures 8 and 9, we removed points from the traces during spiking by eliminating points at which the absolute value of the first temporal derivative of the current trace exceeded $0.005~\mu\text{A/ms·cm}^2$ for the net current, $0.15~\mu\text{A/ms·cm}^2$ for the TRPM4 current, and $0.2~\mu\text{A/ms·cm}^2$ for the NaV current. Points outside the range of -0.3 to $0.09~\mu\text{A/cm}^2$ in the net current trace, greater than $0~\mu\text{A/cm}^2$ in the TRPM4 trace and less than -10 μ A in the Nav current were also removed. Points were removed from the occupancy in O trace if the absolute value of the first temporal derivative of the O state exceeded 0.00002/ms or when occupancy exceeded 0.0002.

Software accessibility

- 856 Model code is freely available and can be downloaded from ModelDB at:
- http://modeldb.yale.edu/267599,
- 858 access code: cholinergicshift.

859

860

861 **REFERENCES**

- 862 Abbott LF, Blum KI (1996) Functional significance of long-term potentiation for sequence learning and
- 863 prediction. Cereb Cortex N Y N 1991 6:406–416.
- 864 Acquas E, Wilson C, Fibiger HC (1996) Conditioned and unconditioned stimuli increase frontal cortical
- and hippocampal acetylcholine release: effects of novelty, habituation, and fear. J Neurosci Off J Soc
- 866 Neurosci 16:3089-3096.
- Arboit A, Reboreda A, Yoshida M (2020) Involvement of TRPC4 and 5 Channels in Persistent Firing in
- 868 Hippocampal CA1 Pyramidal Cells. Cells 9.
- 869 Ashhad S, Narayanan R (2013) Quantitative interactions between the A-type K + current and inositol
- 870 trisphosphate receptors regulate intraneuronal Ca ²⁺ waves and synaptic plasticity: Transient K ⁺ current
- 871 regulates ER Ca²⁺ release. J Physiol 591:1645–1669.
- Autzen HE, Myasnikov AG, Campbell MG, Asarnow D, Julius D, Cheng Y (2018) Structure of the human
- 873 TRPM4 ion channel in a lipid nanodisc. Science 359:228–232.
- 874 Avignone E, Cherubini E (1999) Muscarinic receptor modulation of GABA-mediated giant depolarizing
- potentials in the neonatal rat hippocampus. J Physiol 518:97–107.
- 876 Aznavour N, Mechawar N, Descarries L (2002) Comparative analysis of cholinergic innervation in the
- 877 dorsal hippocampus of adult mouse and rat: A quantitative immunocytochemical study. Hippocampus
- 878 12:206–217.
- Azouz R, Jensen MS, Yaari Y (1994) Muscarinic Modulation of Intrinsic Burst Firing in Rat Hippocampal
- 880 Neurons. Eur J Neurosci 6:961–966.
- 881 Balbi P, Massobrio P, Hellgren Kotaleski J (2017) A single Markov-type kinetic model accounting for the
- 882 macroscopic currents of all human voltage-gated sodium channel isoforms Gillespie D, ed. PLOS
- 883 Comput Biol 13:e1005737.
- 884 Benardo LS, Prince DA (1982) Cholinergic excitation of mammalian hippocampal pyramidal cells. Brain
- 885 Res 249:315-331.
- 886 Bianchi D, Marasco A, Limongiello A, Marchetti C, Marie H, Tirozzi B, Migliore M (2012) On the
- 887 mechanisms underlying the depolarization block in the spiking dynamics of CA1 pyramidal neurons. J
- 888 Comput Neurosci 33:207–225.
- 889 Bianchi L, Ballini C, Colivicchi MA, Della Corte L, Giovannini MG, Pepeu G (2003) Investigation on
- 890 Acetylcholine, Aspartate, Glutamate and GABA Extracellular Levels from Ventral Hippocampus During
- 891 Repeated Exploratory Activity in the Rat. Neurochem Res 28:565–573.

- 892 Bittner KC, Grienberger C, Vaidya SP, Milstein AD, Macklin JJ, Suh J, Tonegawa S, Magee JC (2015)
- 893 Conjunctive input processing drives feature selectivity in hippocampal CA1 neurons. Nat Neurosci
- 894 18:1133–1142.
- 895 Bittner KC, Milstein AD, Grienberger C, Romani S, Magee JC (2017) Behavioral time scale synaptic
- 896 plasticity underlies CA1 place fields. Science 357:1033–1036.
- 897 Bland BH, Colom LV, Konopacki J, Roth SH (1988) Intracellular records of carbachol-induced theta
- rhythm in hippocampal slices. Brain Res 447:364–368.
- 899 Blum KI, Abbott LF (1996) A model of spatial map formation in the hippocampus of the rat. Neural
- 900 Comput 8:85–93.
- 901 Brown DA, Adams PR (1980) Muscarinic suppression of a novel voltage-sensitive K+ current in a
- 902 vertebrate neurone. Nature 283:673–676.
- 903 Buchanan KA, Petrovic MM, Chamberlain SEL, Marrion NV, Mellor JR (2010) Facilitation of long-term
- potentiation by muscarinic M(1) receptors is mediated by inhibition of SK channels. Neuron 68:948–963.
- 905 Burke SN, Maurer AP, Yang Z, Navratilova Z, Barnes CA (2008) Glutamate receptor-mediated
- 906 restoration of experience-dependent place field expansion plasticity in aged rats. Behav Neurosci
- 907 122:535–548.
- 908 Carnevale NT, Hines ML (2006) The NEURON Book. Cambridge University Press.
- 909 Chen S, Benninger F, Yaari Y (2014) Role of Small Conductance Ca2+-Activated K+ Channels in
- 910 Controlling CA1 Pyramidal Cell Excitability. J Neurosci 34:8219–8230.
- 911 Cohen J (1977) CHAPTER 1 The Concepts of Power Analysis. In: Statistical Power Analysis for the
- 912 Behavioral Sciences (Revised Edition), pp 1–17. Academic Press. Available a
- 913 https://www.sciencedirect.com/science/article/pii/B9780121790608500062.
- 914 Colino A, Halliwell JV (1993) Carbachol Potentiates Q Current and Activates a Calcium-dependent Non-
- 915 specific Conductance in Rat Hippocampus In Vitro. Eur J Neurosci 5:1198–1209.
- 916 Combe CL, Canavier CC, Gasparini S (2018) Intrinsic Mechanisms of Frequency Selectivity in the
- 917 Proximal Dendrites of CA1 Pyramidal Neurons. J Neurosci 38:8110–8127.
- 918 Dani JA, Bertrand D (2007) Nicotinic Acetylcholine Receptors and Nicotinic Cholinergic Mechanisms of
- 919 the Central Nervous System. Annu Rev Pharmacol Toxicol 47:699–729.
- 920 Dannenberg H, Young K, Hasselmo M (2017) Modulation of Hippocampal Circuits by Muscarinic and
- 921 Nicotinic Receptors. Front Neural Circuits 11 Available at:
- 922 https://www.frontiersin.org/articles/10.3389/fncir.2017.00102 [Accessed July 29, 2022].
- 923 Dasari S, Gulledge AT (2011) M1 and M4 receptors modulate hippocampal pyramidal neurons. J
- 924 Neurophysiol 105:779–792.
- 925 Dasari S, Hill C, Gulledge AT (2017) A unifying hypothesis for M1 muscarinic receptor signalling in
- 926 pyramidal neurons. J Physiol 595:1711–1723.
- 927 Dienes C, Hézső T, Kiss DZ, Baranyai D, Kovács ZM, Szabó L, Magyar J, Bányász T, Nánási PP,
- 928 Horváth B, Gönczi M, Szentandrássy N (2021) Electrophysiological Effects of the Transient Receptor
- 929 Potential Melastatin 4 Channel Inhibitor (4-Chloro-2-(2-chlorophenoxy)acetamido) Benzoic Acid (CBA) in
- 930 Canine Left Ventricular Cardiomyocytes. Int J Mol Sci 22:9499.

- 931 Disney AA, Higley MJ (2020) Diverse Spatiotemporal Scales of Cholinergic Signaling in the Neocortex. J
- 932 Neurosci 40:720–725.
- 933 Dong C, Madar AD, Sheffield MEJ (2021) Distinct place cell dynamics in CA1 and CA3 encode
- 934 experience in new environments. Nat Commun 12:2977.
- 935 Dutar P, Bassant MH, Senut MC, Lamour Y (1995) The septohippocampal pathway: structure and
- 936 function of a central cholinergic system. Physiol Rev 75:393–427.
- Dutta Banik D, Martin LE, Freichel M, Torregrossa A-M, Medler KF (2018) TRPM4 and TRPM5 are both
- 938 required for normal signaling in taste receptor cells. Proc Natl Acad Sci 115 Available at:
- 939 https://pnas.org/doi/full/10.1073/pnas.1718802115 [Accessed August 5, 2022].
- 940 Easton A, Douchamps V, Eacott M, Lever C (2012) A specific role for septohippocampal acetylcholine in
- 941 memory? Neuropsychologia 50:3156–3168.
- 942 Egorov AV, Hamam BN, Fransén E, Hasselmo ME, Alonso AA (2002) Graded persistent activity in
- 943 entorhinal cortex neurons. Nature 420:173–178.
- 944 Egorov AV, Schumacher D, Medert R, Birnbaumer L, Freichel M, Draguhn A (2019) TRPC channels are
- not required for graded persistent activity in entorhinal cortex neurons. Hippocampus 29:1038–1048.
- 946 Ehrlich BE, Kaftan E, Bezprozvannaya S, Bezprozvanny I (1994) The pharmacology of intracellular
- 947 Ca2+-release channels. Trends Pharmacol Sci 15:145–149.
- 948 Ekstrom AD, Meltzer J, McNaughton BL, Barnes CA (2001) NMDA Receptor Antagonism Blocks
- 949 Experience-Dependent Expansion of Hippocampal "Place Fields." Neuron 31:631–638.
- 950 Epsztein J, Brecht M, Lee AK (2011) Intracellular Determinants of Hippocampal CA1 Place and Silent
- 951 Cell Activity in a Novel Environment. Neuron 70:109–120.
- 952 Fakler B, Adelman JP (2008) Control of K(Ca) channels by calcium nano/microdomains. Neuron 59:873–
- 953 881.
- 954 Fernández de Sevilla D. Núñez A. Buño W (2021) Muscarinic Receptors, from Synaptic Plasticity to its
- 955 Role in Network Activity. Neuroscience 456:60–70.
- 956 Fernandez FR, White JA (2010) Gain Control in CA1 Pyramidal Cells Using Changes in Somatic
- 957 Conductance. J Neurosci 30:230–241.
- 958 Fisahn A, Pike FG, Buhl EH, Paulsen O (1998) Cholinergic induction of network oscillations at 40 Hz in
- 959 the hippocampus in vitro. Nature 394:186–189.
- 960 Frank D, Kafkas A (2021) Expectation-driven novelty effects in episodic memory. Neurobiol Learn Mem
- 961 183:107466.
- 962 Fraser DD, MacVicar BA (1996) Cholinergic-Dependent Plateau Potential in Hippocampal CA1
- 963 Pyramidal Neurons. J Neurosci 16:4113–4128.
- 964 Gafni J, Munsch JA, Lam TH, Catlin MC, Costa LG, Molinski TF, Pessah IN (1997) Xestospongins:
- potent membrane permeable blockers of the inositol 1,4,5-trisphosphate receptor. Neuron 19:723–733.
- 966 Gasparini S, Magee JC (2002) Phosphorylation-dependent differences in the activation properties of
- 967 distal and proximal dendritic Na+ channels in rat CA1 hippocampal neurons. J Physiol 541:665–672.

- 968 Gasparini S, Migliore M (2015) Action Potential Backpropagation. In: Encyclopedia of Computational
- 969 Neuroscience (Jaeger D, Jung R, eds), pp 133-137. New York, NY: Springer. Available at:
- 970 https://doi.org/10.1007/978-1-4614-6675-8 123 [Accessed August 18, 2021].
- 971 Giessel AJ, Sabatini BL (2010) M1 Muscarinic Receptors Boost Synaptic Potentials and Calcium Influx in
- 972 Dendritic Spines by Inhibiting Postsynaptic SK Channels. Neuron 68:936–947.
- 973 Giovannini MG, Rakovska A, Benton RS, Pazzagli M, Bianchi L, Pepeu G (2001) Effects of novelty and
- 974 habituation on acetylcholine, GABA, and glutamate release from the frontal cortex and hippocampus of
- 975 freely moving rats. Neuroscience 106:43–53.
- 976 Gómez-Ocádiz R, Trippa M, Zhang C-L, Posani L, Cocco S, Monasson R, Schmidt-Hieber C (2022) A
- 977 synaptic signal for novelty processing in the hippocampus. Nat Commun 13.
- 978 Gonzales AL, Amberg GC, Earley S (2010) Ca ²⁺ release from the sarcoplasmic reticulum is required for
- 979 sustained TRPM4 activity in cerebral artery smooth muscle cells. Am J Physiol-Cell Physiol 299:C279-
- 980 C288.
- 981 Gonzales AL, Earley S (2012) Endogenous cytosolic Ca2+ buffering is necessary for TRPM4 activity in
- 982 cerebral artery smooth muscle cells. Cell Calcium 51:82–93.
- 983 Guinamard R, Demion M, Launay P (2010) Physiological Roles of the TRPM4 Channel Extracted from
- 984 Background Currents. Physiology 25:155–164.
- 985 Guinamard R, Simard C, Del Negro C (2013) Flufenamic acid as an ion channel modulator. Pharmacol
- 986 Ther 138:272–284.
- 987 Halliwell JV, Adams PR (1982) Voltage-clamp analysis of muscarinic excitation in hippocampal neurons.
- 988 Brain Res 250:71–92.
- 989 Hargreaves EL, Yoganarasimha D, Knierim JJ (2007) Cohesiveness of spatial and directional
- 990 representations recorded from neural ensembles in the anterior thalamus, parasubiculum, medial
- 991 entorhinal cortex, and hippocampus. Hippocampus 17:826–841.
- 992 Harney SC, Rowan M, Anwyl R (2006) Long-Term Depression of NMDA Receptor-Mediated Synaptic
- 993 Transmission Is Dependent on Activation of Metabotropic Glutamate Receptors and Is Altered to Long-
- 994 Term Potentiation by Low Intracellular Calcium Buffering. J Neurosci 26:1128–1132.
- 995 Harvey CD, Collman F, Dombeck DA, Tank DW (2009) Intracellular dynamics of hippocampal place cells
- 996 during virtual navigation. Nature 461:941–946.
- 997 Hasselmo ME (2006) The role of acetylcholine in learning and memory. Curr Opin Neurobiol 16:710-
- 998 715.
- 999 Hines ML, Carnevale NT (1997) The NEURON simulation environment. Neural Comput 9:1179–1209.
- Hoffman DA, Johnston D (1998) Downregulation of Transient K+ Channels in Dendrites of Hippocampal
- 1001 CA1 Pyramidal Neurons by Activation of PKA and PKC. J Neurosci 18:3521–3528.
- Hoffman DA, Magee JC, Colbert CM, Johnston D (1997) K+ channel regulation of signal propagation in
- dendrites of hippocampal pyramidal neurons. Nature 387:869–875.
- Hofmann T, Obukhov AG, Schaefer M, Harteneck C, Gudermann T, Schultz G (1999) Direct activation of
- human TRPC6 and TRPC3 channels by diacylglycerol. Nature 397:259–263.

- 1006 Hou J, Fei Y, Li W, Chen Y, Wang Q, Xiao Y, Wang Y, Li Y (2018) The transient receptor potential
- 1007 melastatin 4 channel inhibitor 9-phenanthrol modulates cardiac sodium channel: 9-Phenanthrol inhibits
- 1008 cardiac sodium channel. Br J Pharmacol 175:4325–4337.
- 1009 Hsu C-L, Zhao X, Milstein AD, Spruston N (2018) Persistent Sodium Current Mediates the Steep Voltage
- Dependence of Spatial Coding in Hippocampal Pyramidal Neurons. Neuron 99:147-162.e8.
- Huerta PT, Lisman JE (1995) Bidirectional synaptic plasticity induced by a single burst during cholinergic
- theta oscillation in CA1 in vitro. Neuron 15:1053–1063.
- 1013 Huff AE, McGraw SD, Winters BD (2022) Muscarinic (M1) cholinergic receptor activation within the
- 1014 dorsal hippocampus promotes destabilization of strongly encoded object location memories.
- 1015 Hippocampus 32:55–66.
- Hutchison IC, Rathore S (2015) The role of REM sleep theta activity in emotional memory. Front Psychol
- 1017 6 Available at: http://journal.frontiersin.org/article/10.3389/fpsyg.2015.01439 [Accessed August 26,
- 1018 2022].
- 1019 Isokawa M, Alger BE (2006) Ryanodine Receptor Regulates Endogenous Cannabinoid Mobilization in
- the Hippocampus. J Neurophysiol 95:3001–3011.
- 1021 Knauer B, Jochems A, Valero-Aracama MJ, Yoshida M (2013) Long-lasting intrinsic persistent firing in rat
- 1022 CA1 pyramidal cells: A possible mechanism for active maintenance of memory: Long-Lasting Persistent
- Firing in Ca1 Pyramidal Cells. Hippocampus 23:820–831.
- 1024 Kopsick JD, Hartzell K, Lazaro H, Nambiar P, Hasselmo ME, Dannenberg H (2022) Temporal dynamics
- of cholinergic activity in the septo-hippocampal system. Front Neural Circuits 16:957441.
- 1026 Launay P, Fleig A, Perraud A-L, Scharenberg AM, Penner R, Kinet J-P (2002) TRPM4 Is a Ca2+-
- 1027 Activated Nonselective Cation Channel Mediating Cell Membrane Depolarization. Cell 109:397–407.
- 1028 Lee I. Griffin AL. Zilli EA. Eichenbaum H. Hasselmo ME (2006) Gradual translocation of spatial correlates
- of neuronal firing in the hippocampus toward prospective reward locations. Neuron 51:639–650.
- 1030 Lei Y-T, Thuault SJ, Launay P, Margolskee RF, Kandel ER, Siegelbaum SA (2014) Differential
- 1031 contribution of TRPM4 and TRPM5 nonselective cation channels to the slow afterdepolarization in
- 1032 mouse prefrontal cortex neurons. Front Cell Neurosci 8 Available at:
- http://journal.frontiersin.org/article/10.3389/fncel.2014.00267/abstract.
- 1034 Levey A, Edmunds S, Koliatsos V, Wiley R, Heilman C (1995) Expression of m1-m4 muscarinic
- 1035 acetylcholine receptor proteins in rat hippocampus and regulation by cholinergic innervation. J Neurosci
- 1036 15:4077–4092.
- 1037 Li K, Abbott SBG, Shi Y, Eggan P, Gonye EC, Bayliss DA (2021) TRPM4 mediates a subthreshold
- 1038 membrane potential oscillation in respiratory chemoreceptor neurons that drives pacemaker firing and
- 1039 breathing. Cell Rep 34:108714.
- 1040 Lin EC, Combe CL, Gasparini S (2017) Differential Contribution of Ca2+-Dependent Mechanisms to
- 1041 Hyperexcitability in Layer V Neurons of the Medial Entorhinal Cortex. Front Cell Neurosci 11:182.
- 1042 Losonczy A, Makara JK, Magee JC (2008) Compartmentalized dendritic plasticity and input feature
- 1043 storage in neurons. Nature 452:436–441.
- 1044 Magee JC (1998) Dendritic Hyperpolarization-Activated Currents Modify the Integrative Properties of
- Hippocampal CA1 Pyramidal Neurons. J Neurosci 18:7613–7624.

- 1046 Mainen ZF, Sejnowski TJ (1995) Reliability of Spike Timing in Neocortical Neurons. Science 268:1503–
- 1047 1506.
- 1048 Martina M, Schultz JH, Ehmke H, Monyer H, Jonas P (1998) Functional and Molecular Differences
- 1049 between Voltage-Gated K ⁺ Channels of Fast-Spiking Interneurons and Pyramidal Neurons of Rat
- 1050 Hippocampus. J Neurosci 18:8111–8125.
- 1051 Masoli S, Tognolina M, Laforenza U, Moccia F, D'Angelo E (2020) Parameter tuning differentiates
- 1052 granule cell subtypes enriching transmission properties at the cerebellum input stage. Commun Biol
- 1053 3:222.
- 1054 Mederos Y Schnitzler M, Gudermann T, Storch U (2018) Emerging Roles of Diacylglycerol-Sensitive
- 1055 TRPC4/5 Channels. Cells 7.
- 1056 Megías M, Emri Z, Freund TF, Gulyás AI (2001) Total number and distribution of inhibitory and excitatory
- 1057 synapses on hippocampal CA1 pyramidal cells. Neuroscience 102:527–540.
- 1058 Mehta MR, Quirk MC, Wilson MA (2000) Experience-Dependent Asymmetric Shape of Hippocampal
- 1059 Receptive Fields. Neuron 25:707–715.
- 1060 Menigoz A, Ahmed T, Sabanov V, Philippaert K, Pinto S, Kerselaers S, Segal A, Freichel M, Voets T,
- Nilius B, Vennekens R, Balschun D (2016) TRPM4-dependent post-synaptic depolarization is essential
- 1062 for the induction of NMDA receptor-dependent LTP in CA1 hippocampal neurons. Pflüg Arch Eur J
- 1063 Physiol 468:593–607.
- 1064 Micheau J, Marighetto A (2011) Acetylcholine and memory: A long, complex and chaotic but still living
- relationship. Behav Brain Res 221:424–429.
- 1066 Mickus T, Jung H, Spruston N (1999) Properties of Slow, Cumulative Sodium Channel Inactivation in Rat
- Hippocampal CA1 Pyramidal Neurons. Biophys J 76:846–860.
- 1068 Mironov SL (2008) Metabotropic glutamate receptors activate dendritic calcium waves and TRPM
- 1069 channels which drive rhythmic respiratory patterns in mice: mGluR, TRPM4 channels, calcium waves
- and inspiratory bursts. J Physiol 586:2277–2291.
- 1071 Nilius B, Mahieu F, Prenen J, Janssens A, Owsianik G, Vennekens R, Voets T (2006) The Ca2+-
- activated cation channel TRPM4 is regulated by phosphatidylinositol 4,5-biphosphate. EMBO J 25:467–
- 1073 478.
- 1074 Nilius B, Prenen J, Droogmans G, Voets T, Vennekens R, Freichel M, Wissenbach U, Flockerzi V (2003)
- 1075 Voltage dependence of the Ca2+-activated cation channel TRPM4. J Biol Chem 278:30813–30820.
- 1076 Nilius B, Prenen J, Janssens A, Voets T, Droogmans G (2004) Decavanadate modulates gating of
- 1077 TRPM4 cation channels: Decavanadate modulates TRPM4. J Physiol 560:753–765.
- Nilius B, Prenen J, Tang J, Wang C, Owsianik G, Janssens A, Voets T, Zhu MX (2005) Regulation of the
- 1079 Ca2+ Sensitivity of the Nonselective Cation Channel TRPM4*. J Biol Chem 280:6423–6433.
- 1080 Nyakas C, Luiten PGM, Spencer DG, Traber J (1987) Detailed projection patterns of septal and diagonal
- band efferents to the hippocampus in the rat with emphasis on innervation of CA1 and dentate gyrus.
- 1082 Brain Res Bull 18:533–545.
- 1083 O'Malley JJ, Seibt F, Chin J, Beierlein M (2020) TRPM4 Conductances in Thalamic Reticular Nucleus
- Neurons Generate Persistent Firing during Slow Oscillations. J Neurosci 40:4813–4823.

- Pace RW, Mackay DD, Feldman JL, Del Negro CA (2007) Inspiratory bursts in the preBötzinger complex
- depend on a calcium-activated non-specific cation current linked to glutamate receptors in neonatal mice:
- 1087 Inspiratory drive potential mechanisms in preBötC neurons. J Physiol 582:113–125.
- 1088 Palacios-Filardo J, Mellor JR (2019) Neuromodulation of hippocampal long-term synaptic plasticity. Curr
- 1089 Opin Neurobiol 54:37–43.
- 1090 Palacios-Filardo J, Udakis M, Brown GA, Tehan BG, Congreve MS, Nathan PJ, Brown AJH, Mellor JR
- 1091 (2021) Acetylcholine prioritises direct synaptic inputs from entorhinal cortex to CA1 by differential
- modulation of feedforward inhibitory circuits. Nat Commun 12:5475.
- 1093 Partridge LD, Valenzuela CF (2000) Block of hippocampal CAN channels by flufenamate. Brain Res
- 1094 867:143–148.
- 1095 Pepeu G, Giovannini MG (2004) Changes in Acetylcholine Extracellular Levels During Cognitive
- 1096 Processes: Table 1. Learn Mem 11:21–27.
- 1097 Picardo MCD, Sugimura YK, Dorst KE, Kallurkar PS, Akins VT, Ma X, Teruyama R, Guinamard R, Kam
- 1098 K, Saha MS, Del Negro CA (2019) Trpm4 ion channels in pre-Bötzinger complex interneurons are
- essential for breathing motor pattern but not rhythm Dubuc R, ed. PLOS Biol 17:e2006094.
- 1100 Poirazi P, Brannon T, Mel BW (2003a) Arithmetic of subthreshold synaptic summation in a model CA1
- 1101 pyramidal cell. Neuron 37:977–987.
- 1102 Poirazi P, Brannon T, Mel BW (2003b) Pyramidal Neuron as Two-Layer Neural Network. Neuron
- 1103 37:989–999.
- 1104 Priestley JB, Bowler JC, Rolotti SV, Fusi S, Losonczy A (2022) Signatures of rapid plasticity in
- 1105 hippocampal CA1 representations during novel experiences. Neuron 110:1978-1992.e6.
- 1106 Provence A, Rovner ES, Petkov GV (2017) Regulation of transient receptor potential melastatin 4
- 1107 channel by sarcoplasmic reticulum inositol trisphosphate receptors: Role in human detrusor smooth
- 1108 muscle function. Channels Austin Tex 11:459–466.
- 1109 Putney JW (2005) Physiological mechanisms of TRPC activation. Pflüg Arch Eur J Physiol 451:29–34.
- 1110 Raymond CR, Redman SJ (2006) Spatial segregation of neuronal calcium signals encodes different
- 1111 forms of LTP in rat hippocampus. J Physiol 570:97–111.
- 1112 Reboreda A, Jiménez-Díaz L, Navarro-López JD (2011) TRP Channels and Neural Persistent Activity. In:
- 1113 Transient Receptor Potential Channels (Islam MdS, ed), pp 595–613 Advances in Experimental Medicine
- and Biology. Dordrecht: Springer Netherlands. Available at: http://link.springer.com/10.1007/978-94-007-
- 1115 0265-3_32 [Accessed August 9, 2022].
- 1116 Resnik E, McFarland JM, Sprengel R, Sakmann B, Mehta MR (2012) The effects of GluA1 deletion on
- the hippocampal population code for position. J Neurosci Off J Soc Neurosci 32:8952–8968.
- 1118 Riquelme D, Cerda O, Leiva-Salcedo E (2021) TRPM4 Expression During Postnatal Developmental of
- 1119 Mouse CA1 Pyramidal Neurons. Front Neuroanat 15:643287.
- 1120 Roth ED, Yu X, Rao G, Knierim JJ (2012) Functional Differences in the Backward Shifts of CA1 and CA3
- 1121 Place Fields in Novel and Familiar Environments Gilestro GF, ed. PLoS ONE 7:e36035.

- 1122 Sahu G, Turner RW (2021) The Molecular Basis for the Calcium-Dependent Slow Afterhyperpolarization
- 1123 in CA1 Hippocampal Pyramidal Neurons. Front Physiol 12 Available at:
- https://www.frontiersin.org/articles/10.3389/fphys.2021.759707.
- 1125 Sarter M, Lustig C (2020) Forebrain Cholinergic Signaling: Wired and Phasic, Not Tonic, and Causing
- 1126 Behavior. J Neurosci 40:712–719.
- 1127 Savelli F, Knierim JJ (2010) Hebbian analysis of the transformation of medial entorhinal grid-cell inputs to
- hippocampal place fields. J Neurophysiol 103:3167–3183.
- 1129 Shah MM, Migliore M, Valencia I, Cooper EC, Brown DA (2008) Functional significance of axonal Kv7
- channels in hippocampal pyramidal neurons. Proc Natl Acad Sci 105:7869–7874.
- 1131 Simard C, Sallé L, Rouet R, Guinamard R (2012) Transient receptor potential melastatin 4 inhibitor 9-
- 1132 phenanthrol abolishes arrhythmias induced by hypoxia and re-oxygenation in mouse ventricle: Anti-
- arrhythmic effect of 9-phenanthrol. Br J Pharmacol 165:2354–2364.
- 1134 Takács VT, Cserép C, Schlingloff D, Pósfai B, Szőnyi A, Sos KE, Környei Z, Dénes Á, Gulyás AI, Freund
- 1135 TF, Nyiri G (2018) Co-transmission of acetylcholine and GABA regulates hippocampal states. Nat
- 1136 Commun 9:2848.
- 1137 Tedoldi A, Ludwig P, Fulgenzi G, Takeshima H, Pedarzani P, Stocker M (2020) Calcium-induced calcium
- 1138 release and type 3 ryanodine receptors modulate the slow afterhyperpolarising current, sIAHP, and its
- potentiation in hippocampal pyramidal neurons. PLOS ONE 15:e0230465.
- 1140 Thiel CM, Huston JP, Schwarting RKW (1998) Hippocampal acetylcholine and habituation learning.
- 1141 Neuroscience 85:1253–1262.
- 1142 Upchurch CM, Combe CL, Knowlton CJ, Rousseau VG, Gasparini S, Canavier CC (2022) Long-Term
- 1143 Inactivation of Sodium Channels as a Mechanism of Adaptation in CA1 Pyramidal Neurons. J Neurosci
- 1144 42:3768–3782.
- 1145 Venkatesan K, Liu Y, Goldfarb M (2014) Fast-Onset Long-Term Open-State Block of Sodium Channels
- 1146 by A-type FHFs Mediates Classical Spike Accommodation in Hippocampal Pyramidal Neurons. J
- 1147 Neurosci 34:16126–16139.
- 1148 Venugopal S, Hsiao C-F, Sonoda T, Wiedau-Pazos M, Chandler SH (2015) Homeostatic dysregulation in
- 1149 membrane properties of masticatory motoneurons compared with oculomotor neurons in a mouse model
- 1150 for amyotrophic lateral sclerosis. J Neurosci Off J Soc Neurosci 35:707–720.
- 1151 Veress R, Baranyai D, Hegyi B, Kistamás K, Dienes C, Magyar J, Bányász T, Nánási PP, Szentandrássy
- 1152 N, Horváth B (2018) Transient receptor potential melastatin 4 channel inhibitor 9-phenanthrol inhibits K
- but not Ca ²⁺ currents in canine ventricular myocytes. Can J Physiol Pharmacol 96:1022–1029.
- 1154 Vierra NC, Kirmiz M, van der List D, Santana LF, Trimmer JS (2019) Kv2.1 mediates spatial and
- 1155 functional coupling of L-type calcium channels and ryanodine receptors in mammalian neurons Swartz
- 1156 KJ, Marder E, eds. eLife 8:e49953.
- 1157 Yamada-Hanff J, Bean BP (2013) Persistent sodium current drives conditional pacemaking in CA1
- 1158 pyramidal neurons under muscarinic stimulation. J Neurosci 33:15011–15021.
- 1159 Yamasaki M, Matsui M, Watanabe M (2010) Preferential Localization of Muscarinic M1 Receptor on
- 1160 Dendritic Shaft and Spine of Cortical Pyramidal Cells and Its Anatomical Evidence for Volume
- 1161 Transmission. J Neurosci 30:4408–4418.

- 1162 Yoshida M, Knauer B, Jochems A (2012) Cholinergic modulation of the CAN current may adjust neural
- 1163 dynamics for active memory maintenance, spatial navigation and time-compressed replay. Front Neural
- Circuits 6 Available at: http://journal.frontiersin.org/article/10.3389/fncir.2012.00010/abstract. 1164
- Zhang Z. Reboreda A. Alonso A. Barker PA, Séguéla P (2011) TRPC channels underlie cholinergic 1165
- plateau potentials and persistent activity in entorhinal cortex. Hippocampus 21:386–397. 1166
- 1167 Zhu MX (2005) Multiple roles of calmodulin and other Ca2+-binding proteins in the functional regulation
- 1168 of TRP channels. Pflüg Arch - Eur J Physiol 451:105-115.

1170 Figure legends

1169

1195

- 1171 Figure 1. Carbachol shifts the center of mass of firing in response to depolarizing current ramps.
- 1172 A. Somatic recording, control. A1. Voltage trace for a two second triangular current ramp (represented
- 1173 below) injected in the soma. A2. Instantaneous frequency for example in A1 as it changes along the
- 1174 ramp. A3. Raster plot of different trials recorded from the same example neuron in A1. The trials are
- 1175 ordered by the amplitude of the peak injected current, from lowest (bottom) to highest (top); trials with the
- 1176 same amount of current injection are clustered together. B. Somatic recording, carbachol. B1, B2, and
- 1177 B3. Same as A1, A2, and A3, but during superfusion with 2 µM CCh, C1. Instantaneous frequency for
- 1178 example in A1, as it changes with injected current. Filled circles represent firing on the up-ramp; open
- 1179 circles, firing on the down-ramp. C2. Instantaneous frequency for example in B1. A, B, and C are
- 1180 recordings from the same cell. D. Summary data of the adaptation index for somatic recordings, before
- 1181 and during CCh, for two second ramps (n = 21) and ten second ramps (n = 19). Open circles connected
- 1182 by gray lines represent indices for individual cells, before and during CCh. Black squares with error bars
- 1183 represent group averages ± SEM. In control, all adaptation indices are positive, indicating more action
- 1184 potentials on the up-ramp. In CCh. most adaptation indices are negative, indicating more action
- 1185 potentials on the down-ramp. E. Dendritic recording, control. E1. Voltage trace for a two second
- 1186 triangular current ramp (represented below) injected in the dendrite, approximately 200 µm from the
- 1187 soma. E2. Instantaneous frequency for E1 as it changes along the ramp. E3. Raster plot of different trials
- recorded from same example neuron in E1. F. Dendritic recording, carbachol. F1, F2, and F3. Same as
- 1188
- 1189 E1, E2, and E3, but during superfusion with 2 µM CCh. G1. Instantaneous frequency for example in E1,
- 1190 as it changes with injected current. G2. Instantaneous frequency for example in F1. E, F, and G are from
- 1191 the same cell. H. Summary data of the adaptation index for dendritic ramps, before and during CCh, for
- two second ramps (n = 19) and ten second ramps (n = 10). *** p < 0.0005. Red dotted lines in the left 1192
- 1193 panels mark the middle of the current injection ramp. Source data in "Figure 1 - Source data". See also
- 1194 Figure 1 – supplement 1 and Figure 1 – supplement 2.
- 1196 Figure 2. Cholinergic modulation of the response to electrical stimulation of Schaffer collaterals, recorded
- 1197 at the soma. A Top, synaptic response in control conditions to an input frequency that increases and
- 1198 decreases symmetrically, from 6.7 to 25 Hz, as denoted by the pulses under the voltage trace. Bottom,

Raster plot of multiple trials repeated at the same stimulation intensity. B same as A during superfusion of 2 μ M CCh. A and B are from the same neuron, and at the same stimulation intensity. Diamonds in A and B point to a longer EPSP decay time in the presence of CCh. C. Summary data of the adaptation index for synaptic ramps, before and during CCh. D. Summary data of the average EPSP amplitude measured during trials where the cells did not fire in response to the first stimulus pulse, before and during CCh. In both cases, open circles connected by gray lines represent indices for individual cells; black squares with error bars represent group averages \pm SEM *** p < 0.0005, ** p = 0.002. Red dotted lines in the panels on the left mark the middle of the synaptic stimulation. Source data in "Figure 2 - Source data".

Figure 3. Modulation of response to symmetric ramps by acetylcholine is concentration dependent.

A. Voltage trace recorded in the soma for a two second triangular current ramp injected in the soma in control. Current traces and instantaneous frequency plots are just below the voltage traces. B-D. Same as A, during superfusion with 2 μ M ACh (B), 10 μ M ACh (C), and 15 μ M ACh (D). A through D are from the same cell. E. Summary data of the adaptation index for control and the three concentrations of ACh, applied in order of increasing concentration (n = 13). Open circles connected by gray lines represent indices for individual cells over all four conditions. Black squares with error bars represent group averages \pm SEM. *** p < 0.0005, ** p = 0.001, * p = 0.01. Red dotted lines in the panels on the left mark the middle of the current injection ramp. Source data in "Figure 3 - Source data".

Figure 4. Cholinergic-associated shift in the timing of firing on ramp is mediated by TRP channels, but notably not TRPC channels. A. Somatic recordings for a two second triangular current ramp injected in the soma in control (A1), CCh (2 μ M, A2), and CCh + FFA (100 μ M, A3) applied subsequently to the same cell. Current traces and instantaneous frequency plots are just below the voltage traces. Summary data (A4) of the adaptation index for control, CCh, and CCh + FFA (n = 9). B. Same as in A, but for dendritic injection and recordings. Summary data (B4) of the adaptation index for control, CCh, and CCh + FFA (n = 9). Open circles connected by gray lines represent indices for individual cells, over all three treatments. Black squares with error bars represent group averages \pm SEM. C. Somatic recordings for a two second triangular current ramp injected in the soma in control (C1), CCh (2 μ M, C2), and CCh + SKF96365 (50 μ M, C3) applied subsequently to the same cell. Current traces and instantaneous frequency plots are just below voltage traces. Red dotted line marks the middle of the ramp. Summary data (C4) of the adaptation index for control, CCh, and CCh + SKF96365 (n = 8). D. Same as in C, but for dendritic injection and recordings. Summary data (D4) of the adaptation index for control, CCh, and CCh + SKF96365 (n = 8). **** p < 0.0005, *** p = 0.001, ** p = 0.02, n.s. not significant. Source data in "Figure 4 - Source data".

Figure 5. Cholinergic-mediated shift in the center of mass of firing is mediated by TRPM4 channels.

A. Somatic recordings for a two second triangular current ramp injected in the soma in control (A1), CCh (2 μ M, A2), and CCh + CBA (50 μ M, A3) applied subsequently to the same cell. Current traces and instantaneous frequency plots are just below voltage traces. Red dotted line marks the middle of the ramp. Summary data (A4) of the adaptation index for control, CCh, and CCh + CBA (n = 9). Open circles connected by gray lines represent indices for individual cells, over all three treatments. Black squares with error bars represent group averages \pm SEM. B. Same as in A, but for dendritic injection and recordings. Summary data (B4) of the adaptation index for control, CCh, and CCh + CBA (n = 9). C. Same as A, but for control (C1), CCh (2 μ M, C2), and CCh + 9-phenanthrol (100 μ M, C3) applied subsequently to the same cell. Summary data (C4) of the adaptation index for control, CCh, and CCh + 9-phenanthrol (n = 8). *** p < 0.0005, ** p = 0.002, * p = 0.002, ## p = 0.001, # p = 0.03, n.s. not significant. Source data in "Figure 5 - Source data".

Figure 6. Pharmacological block of IP₃R or RyRs has no effect on CCh-mediated shift in firing along ramp.

A. Somatic recordings during intracellular dialysis with Xestospongin C (2 μ M), for a two second triangular current ramp injected in the soma before (A1), and during superfusion with CCh (2 μ M, A2). Current traces and instantaneous frequency plots are just below voltage traces. Summary data (A3) of the adaptation index for Xestospongin C (1-2 μ M) and CCh (n = 9). Circles connected by gray lines represent ratios for individual cells, before and during CCh. Filled circles represent cells dialyzed with 1 μ M Xestospongin C and open circles represent cells dialyzed with 2 μ M Xestospongin C. Black squares with error bars represent group averages \pm SEM. B. Same as A, but intracellular dialysis is with ryanodine (40 μ M). Summary data (B3) of the adaptation index for ryanodine and CCh (n = 9). Individual cells represented by open circles. *** p < 0.0005. In both sets of experiments, control data reflect the effect of either IP₃R or RyR antagonist before the addition of CCh, because the dialysis started to be apparent quickly after break-in. Red dotted lines in the left panels mark the middle of the ramp. C1 and C2. Same as B1 and B2; C3 is an expanded version of the inset in C1. Source data in "Figure 6 - Source data".

Figure 7. A. Simulated control response to triangular current ramp. A1. Top. Simplified model calcium handling schematic. For simplicity, only one annulus (shell) is shown, and the rest are represented as the core. Ca²⁺ enters via voltage-gated Ca²⁺ channels (Ca_V) and is removed by the plasma membrane Ca²⁺ ATPase (PMCA) pump. Inside the cell, buffering and the endoplasmic reticulum (ER) are also modeled. The TRPM4 channel is not permeable to Ca²⁺ and senses [Ca²⁺] in a nanodomain (ND). In the control simulation, the nanodomain is contiguous with the cytosol. Bottom trace shows the voltage responses, plotted in the somatic compartment, to a triangular current ramp applied in the soma (shown below). A2.

Ca²⁺ concentration (in nM) in the outermost shell of the somatic compartment. A3. The nanodomain Ca²⁺ concentration (same as the that of the outer shell in A2 in this case) is negligible when plotted in μM scale. A4. TRPM4 activation is negligible in control. B. Simulated response to triangular current ramp during simulated application of CCh. B1. As in A1 except for ligand (magenta dot) binding to the metabotropic acetylcholine receptor (mAChR), triggering Ca²⁺ influx into a nanodomain linked to the TRPM4 channel. The voltage trace shows that the center of mass of firing is shifted to later times. B2. Ca²⁺ concentration (in nM) in the outermost shell of the somatic compartment. B3. In contrast to control, the addition of a nanodomain with privileged Ca²⁺ access allows micromolar concentrations to be reached and sensed by TRPM4 channels. B4. In contrast to control, TRPM4 is now activated during the ramp. Vertical dashed red line shows the peak of the current ramp.

Figure 8. The model explains how simulated TRPM4 channel activation can reverse the adaptation mediated by long-term inactivation of Na_V1.6 channels. A. Voltage traces from 7A1 and B1 overlaid; control (in black), CCh (in magenta). The triangular current injection ramps are shown below. B. Occupancy of Na_V1.6 channel in the open state (O) in the somatic compartment, with values during spikes removed. C. Occupancy of Na_V1.6 channel in the long-term inactivated state (I2). D. Persistent Na_V current (spiking values removed) E. TRPM4 current. F. Net ionic current. All values are shown for somatic compartment.

 Figure 9. The model explains how activation of TRPM4 channels affects the firing pattern in response to triangular ramps that evoke similar firing frequencies. A. Simulated voltage traces (top) during a two second triangular current ramp (just below voltage traces). Insets show the reciprocal of the interspike interval (ISI) plotted as the instantaneous frequency at the ISI midpoint. Vertical dashed red line shows the peak of the current ramp. The slower frequencies at similar values of injected current and fewer ISIs on the down-ramp (open circles) versus the up-ramp (closed circles) in control show hysteresis due to adaptation mediated by long-term inactivation of the sodium channel. TRPM4 channel activation causes the center of mass of firing to be shifted to the right in all other traces compared to control because a nanodomain for TRPM4 activation with special access to Ca2+ was added in simulated CCh. The hysteresis is in the opposite direction because the activation of TRPM4 channels by Ca²⁺ accumulation obscures and overwhelms adaptation. In the light blue traces, the voltage-dependence of TRPM4 activation was not included, so there is less Ca2+ accumulation in the outer shell in B and in the nanodomain in C. resulting in less activation of TRPM4 channels in D. In order to isolate the effect of voltage-dependence from that of Ca²⁺ dependence, the Ca²⁺ waveforms in all nanodomains were recorded during the full CCh simulation shown in magenta, and played back into each nanodomain Ca²⁺ during the simulations shown in purple.

Figure 10. A high concentration of BAPTA is required to interfere with CCh-mediated shift in firing along ramp.

A. Somatic recordings during intracellular dialysis with 10 mM BAPTA, for a two second triangular current ramp injected in the soma before (A1), and during superfusion with CCh (2 μ M, A2). Current traces and instantaneous frequency plots are just below voltage traces. Red dotted line marks the middle of the ramp. Summary data (A3) of the adaptation index for control and CCh (n = 10). Open circles connected by gray lines represent ratios for individual cells, before and during CCh. Black squares with error bars represent group averages \pm SEM. B. Same as A, but intracellular dialysis is with 30 mM BAPTA and 100 nM free [Ca²⁺]. Summary data (B3) of the adaptation index for control and CCh (n = 8). C. Same as A, but intracellular dialysis is with 30 mM BAPTA and 10 nM free [Ca²⁺]. Summary data (C3) of the adaptation index for control and CCh (n = 12). *** p < 0.0005, ** p = 0.001, n.s. not significant. Source data in "Figure 10 - Source data".

1320 Figure 11. Model Schematics.

A. Reconstructed morphology ported to NEURON simulation program, with somatic and dendritic current injection sites labeled. B. Equivalent circuit diagram, with the reversal potentials for each channel indicated by E_X . The following currents were modeled using Ohmic drive and conductances in parallel with a membrane capacitance (C_M): a Na^+ current (I_{Na}), L-type (I_{CaL}), R-type (I_{CaR}), and T-type (I_{CaT}) Ca^{2+} currents, two delayed rectifiers (I_{Kv1} and I_{Kv2}), an A-type K^+ current (I_A), an inward rectifying K^+ current (I_{KIR}), a nonspecific Ca^{2+} -activated current (I_{CAN}), a hyperpolarization-activated mixed cationic h-current (I_h), and a leak current (I_L). C. Markov Model of the NaV channel with an open state (O), a closed state (C), a short-term inactivated state (I1) and a long-term inactivated state (I2). See also Figure 11 – supplement 1.

Figure 1 – supplement 1. Plots of instantaneous frequency versus current injection showing different effects of carbachol on firing rate adaptation. A and B. Two examples of somatic recordings where the firing rate adaptation in control is reversed in the presence of CCh, such that the clockwise hysteresis becomes counter-clockwise. C and D. Two examples of somatic recordings where the firing rate adaptation in control is removed in the presence of CCh, such that the hysteresis disappears, and the motion becomes linear. Filled circles represent the firing frequencies on the up-ramp and open circles represent firing frequencies on the down-ramp.

Figure 1 – supplement 2. A. Adaptation index as a function of membrane potential. Index values for each trial for all neurons are plotted against the membrane potential measured just before the current injection

ramp for that trial, both for somatic recordings (n = 132 in control conditions, filled circles; n = 144 in the presence of CCh 2 μ M, open circles) and for dendritic recordings (n = 135 in control conditions, filled circles; n = 87 during CCh, open circles). B. Adaptation index as a function of the peak injected current. Index values for each trial for all recorded neurons are shown plotted against the peak amplitude of the triangular-shaped current injection for that trial, for both somatic and dendritic recordings (values for n and symbols are the same as in A). C. Adaptation index as a function of input resistance. Average adaptation index values per cell for both somatic recordings (n = 17) and dendritic recordings (n = 12) are plotted against the average steady state input resistance measured during control conditions (filled circles) and during perfusion with CCh (open circles). Source data in "Figure 1 supplement 2 - Source data".

1351

1352

1353

1354

13551356

1357

13581359

1360

1361

13621363

1364

1365

13661367

1341

1342

1343

1344

1345

1346

1347

1348

1349

1350

Figure 11 - supplement 1. Old model in which the source of Ca2+ with privileged access to the nanodomain required to activated TRPM4 channels is IP₃R. This model captures the responses seen with cholinergic activation in the experiments. A. Simulated somatic recordings in control (low IP₃). A1. Voltage traces and current ramp. A2. Nanomolar Ca2+ concentration in outer shell beneath the cell membrane. A3. The nanodomain Ca²⁺ concentration is not elevated with low levels of IP₃ that simulate control. A4. There is negligible TRPM4 activation. B. Simulated somatic recordings in CCh (high IP₃). B1. Voltage traces and current ramp. B2. Nanomolar Ca²⁺ concentration in outer shell beneath the cell membrane is elevated due to increased spiking on the down-ramp. B3. The nanodomain Ca²⁺ concentration reached micromolar concentrations with high levels of IP₃ that simulate application of CCh. B4. TRPM4 is robustly activated. Black dashed line marks the end of the injected current ramp, highlighting that the return to baseline of Ca²⁺ and TRPM4 current lags behind injected current ramp. C. Simulated somatic recordings in CCh (high IP₃) with no nanodomain. C1. Voltage traces and current ramp. Note that more ramp current is required to achieve the same firing rates as were achieved in B1. C2. Nanomolar Ca²⁺ concentration in outer shell beneath the cell membrane. C3. No nanodomain. C4. There is negligible TRPM4 activation. In A2 and C2, the red arrows point to when the [Ca2+] in the outer shell starts decreasing while the neuron keeps firing, as opposed to B2.

somatic injection Α1 **B**1 CCh (2 µM) control C1 C2 frequency (Hz) 20 • up o down 10 20 mV 0 0 180 220 injected current (pA) 110 140 injected current (pA) 140 80 -65 mV 200 pA A2 B2 D 1.0 2 s ramps 10 s ramps Hz 0adaptation index 0.5 А3 **B**3 increasing l_{ramp} increasing l_{ramp} 0.0 -0.5 -1.0 time (s) Ó time (s) CCh CĊh control control dendritic injection E1 CCh (2 µM) control F1 G1 G2 frequency (Hz) • up o down 20 20 mV 0 | 100 0 120 140 injected current (pA) 20 40 injected current (pA) 200 pA 0.5 s 2 s ramps 10 s ramps Η E2 F2 1.0-Hz adaptation index 0-0.5 **E**3 F3 increasing l increasing I ramp 0.0 -0.5 0 CCh control CCh control

Figure 1

time (s)

time (s)

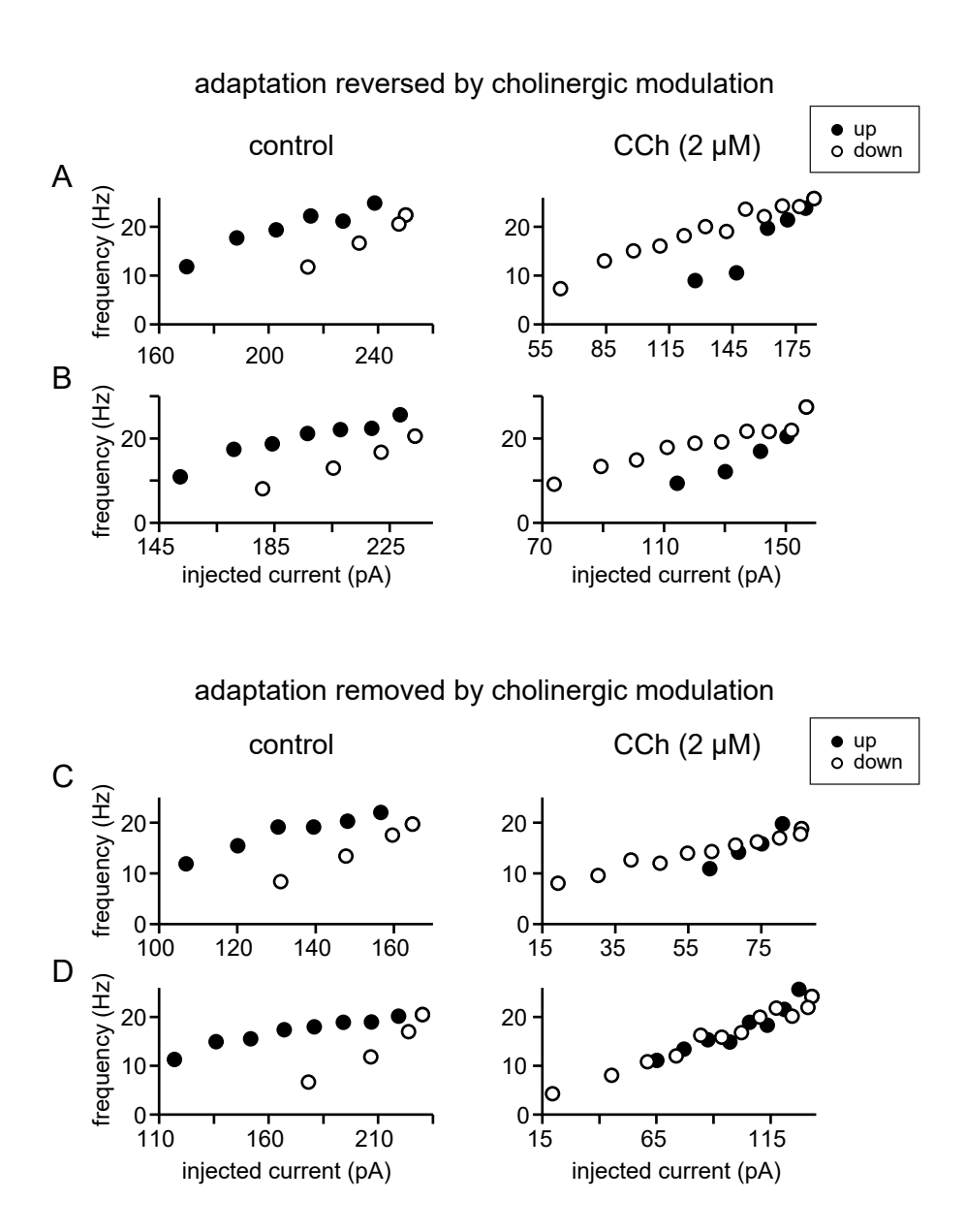
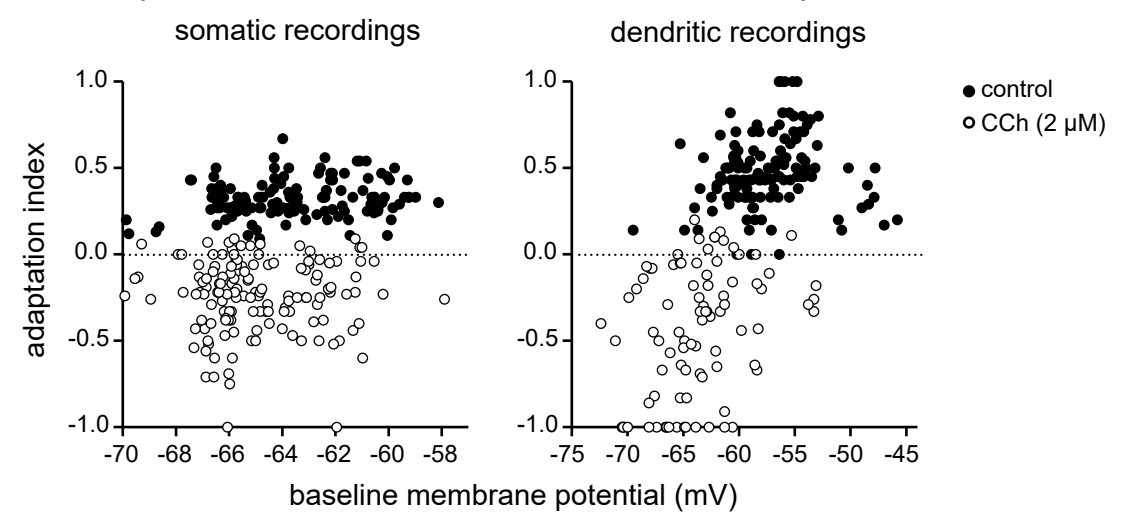
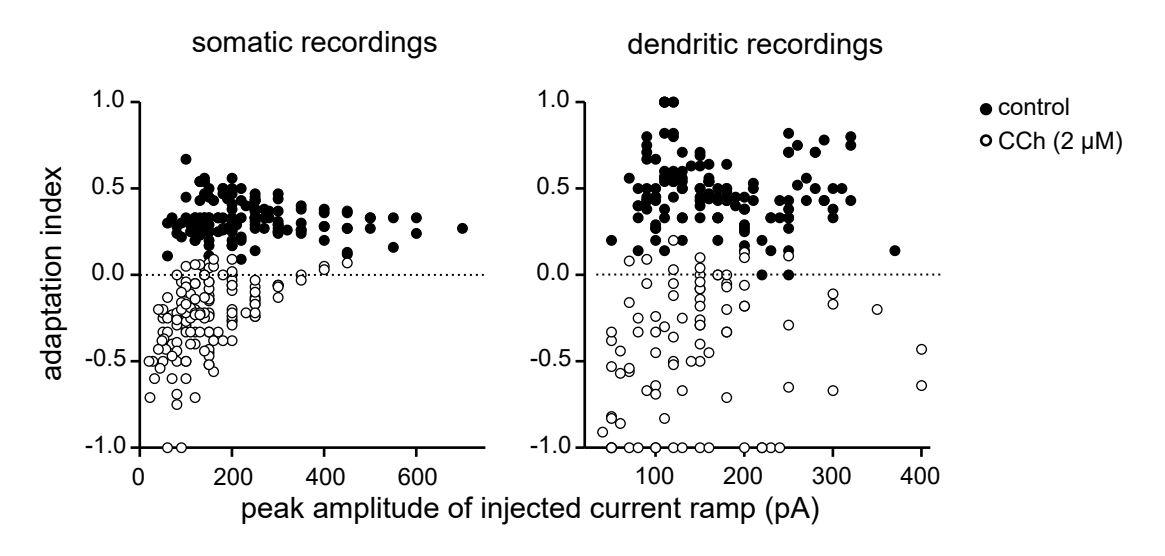


Figure 1 Supplement 1

A adaptation index as a function of initial membrane potential



B adaptation index as a function of current injection amplitude



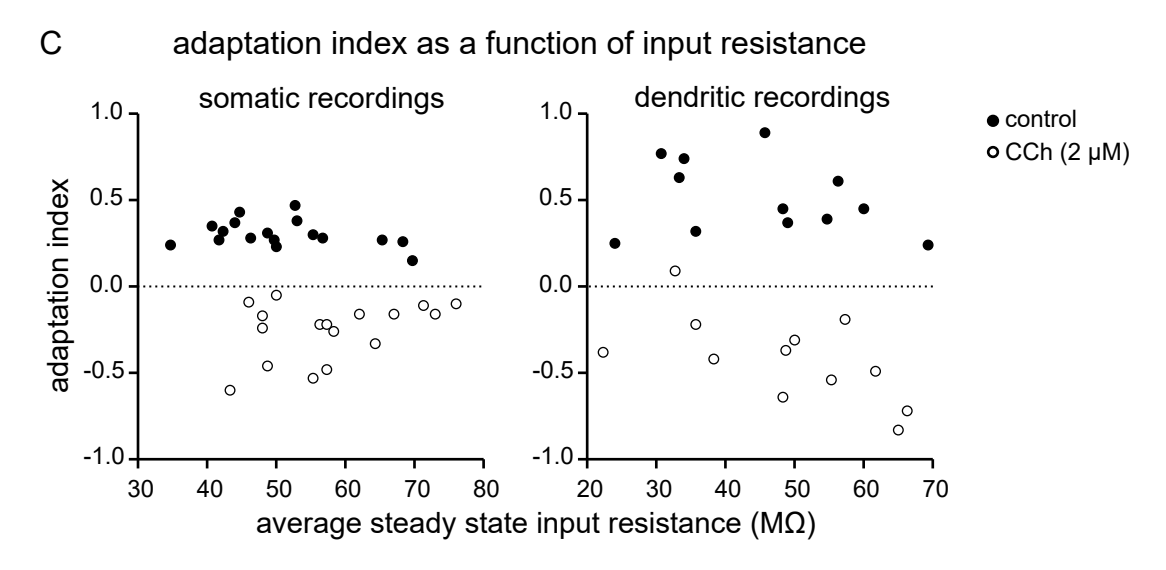


Figure 1 Supplement 2

synaptic stimulation

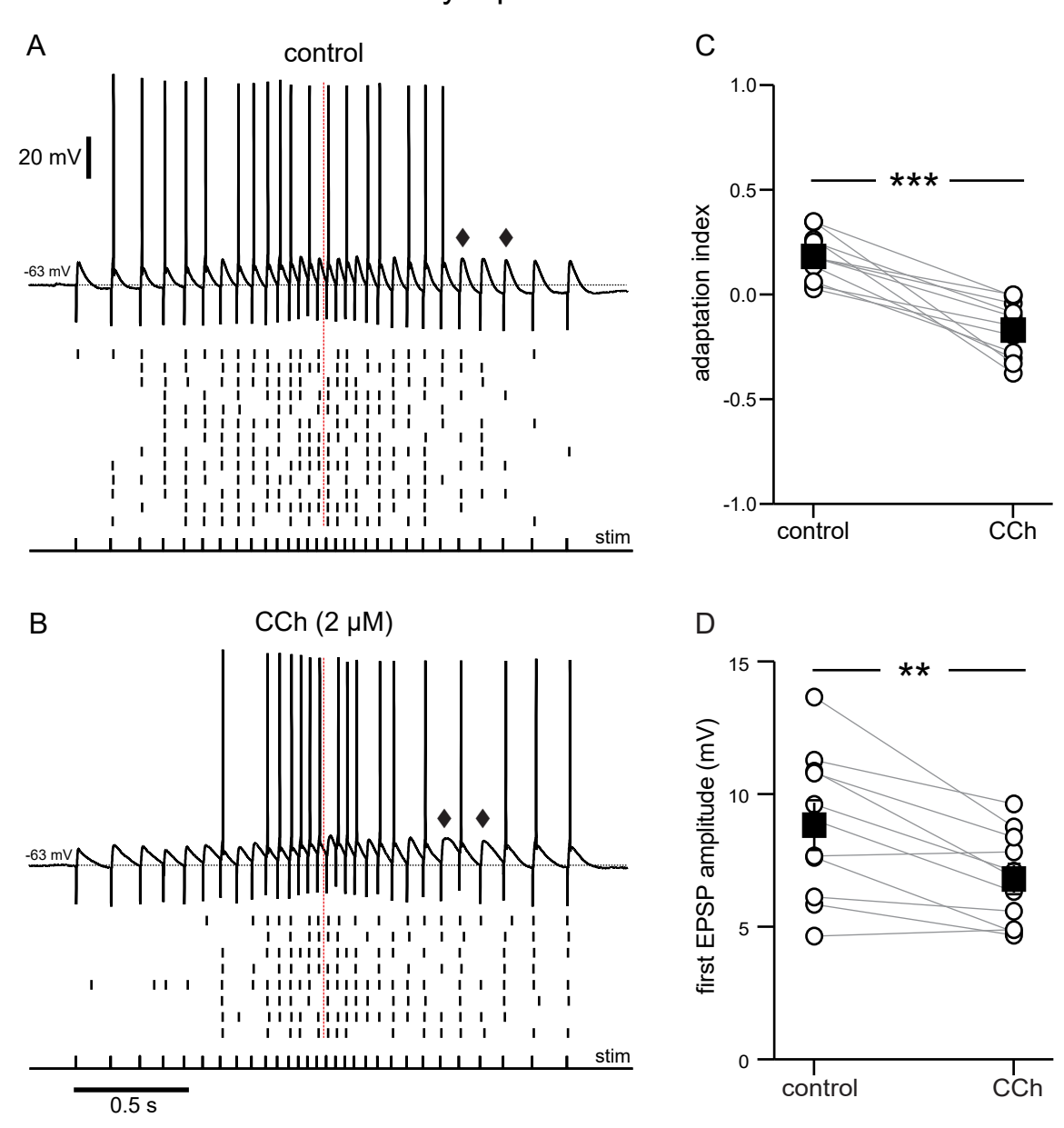


Figure 2

somatic injection

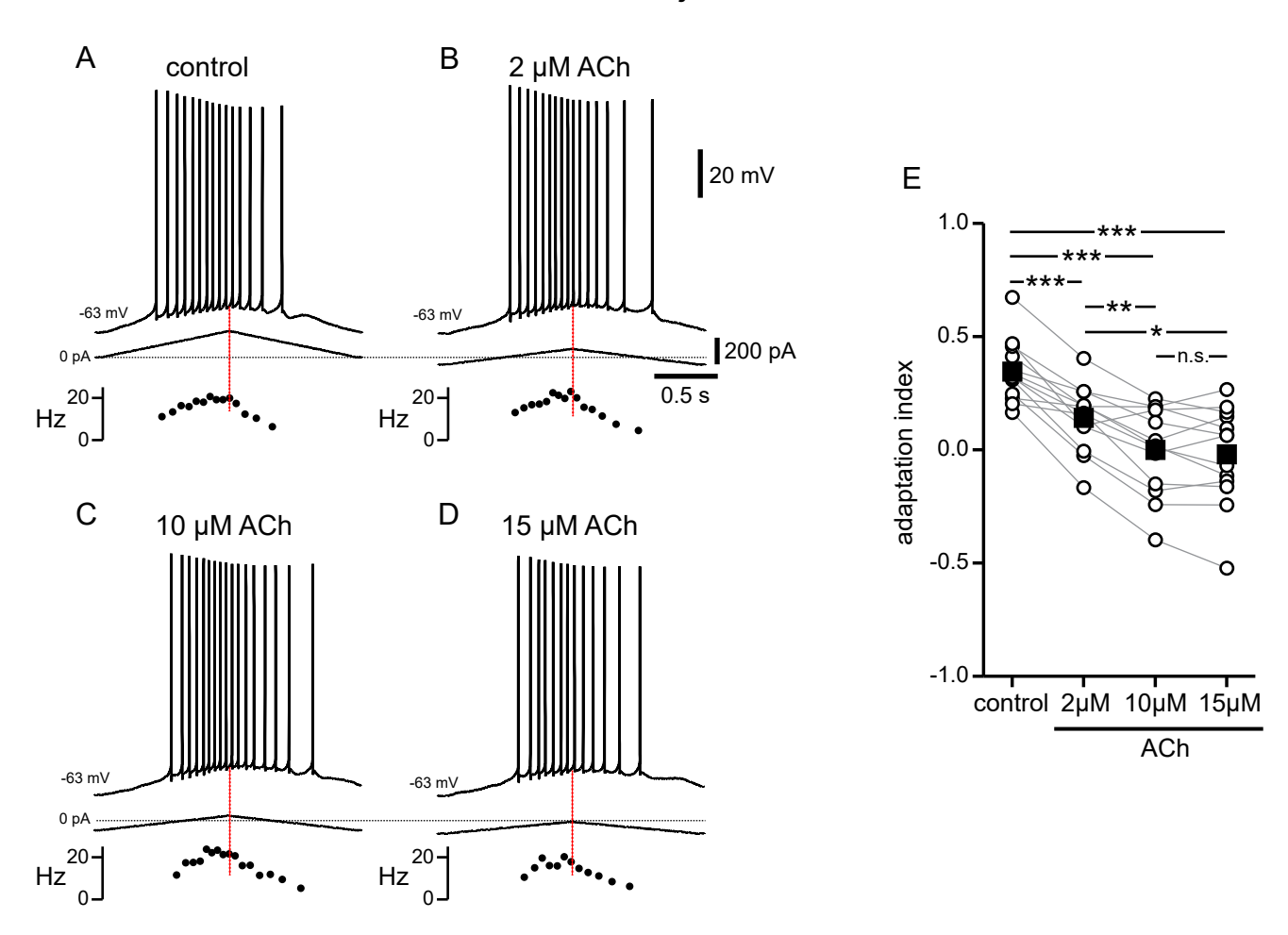
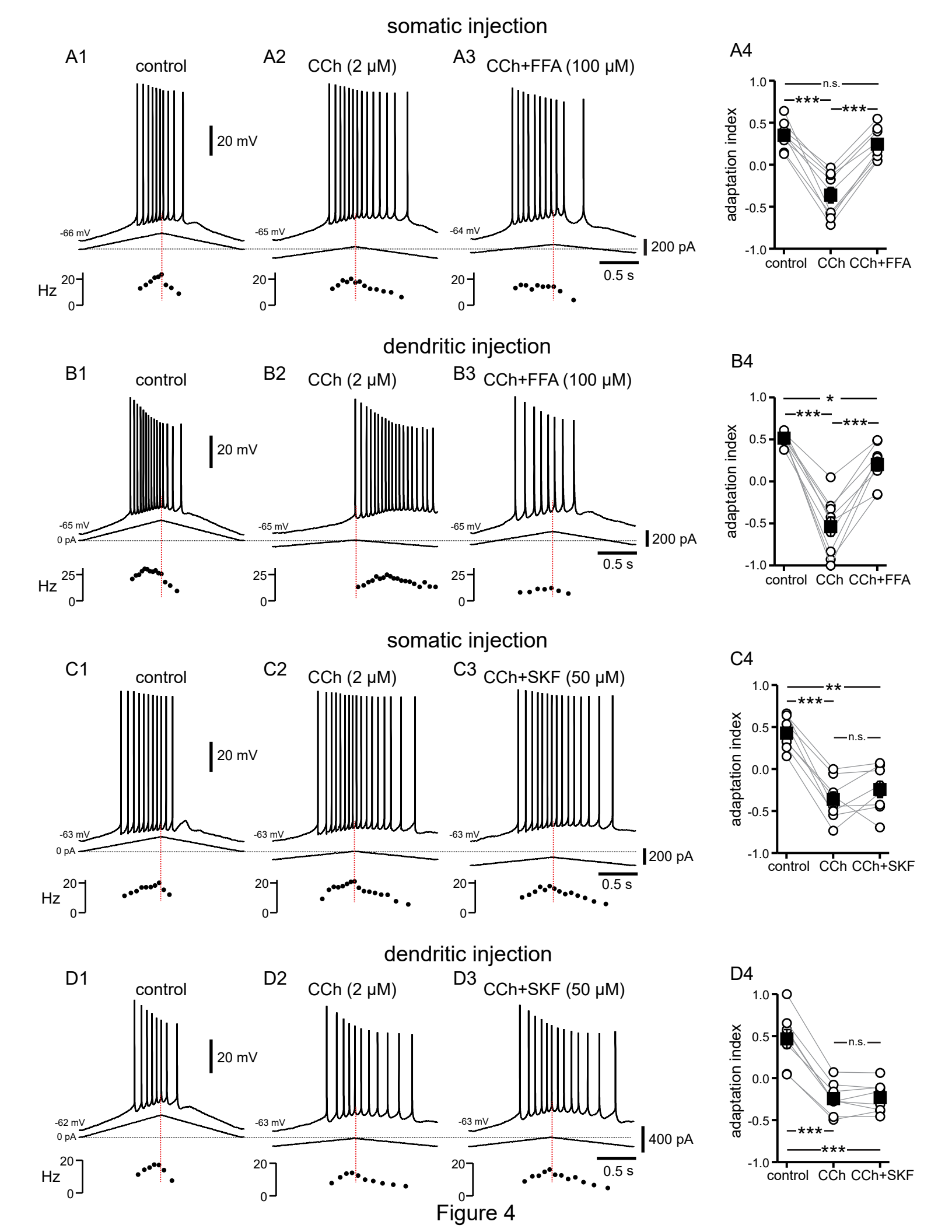


Figure 3



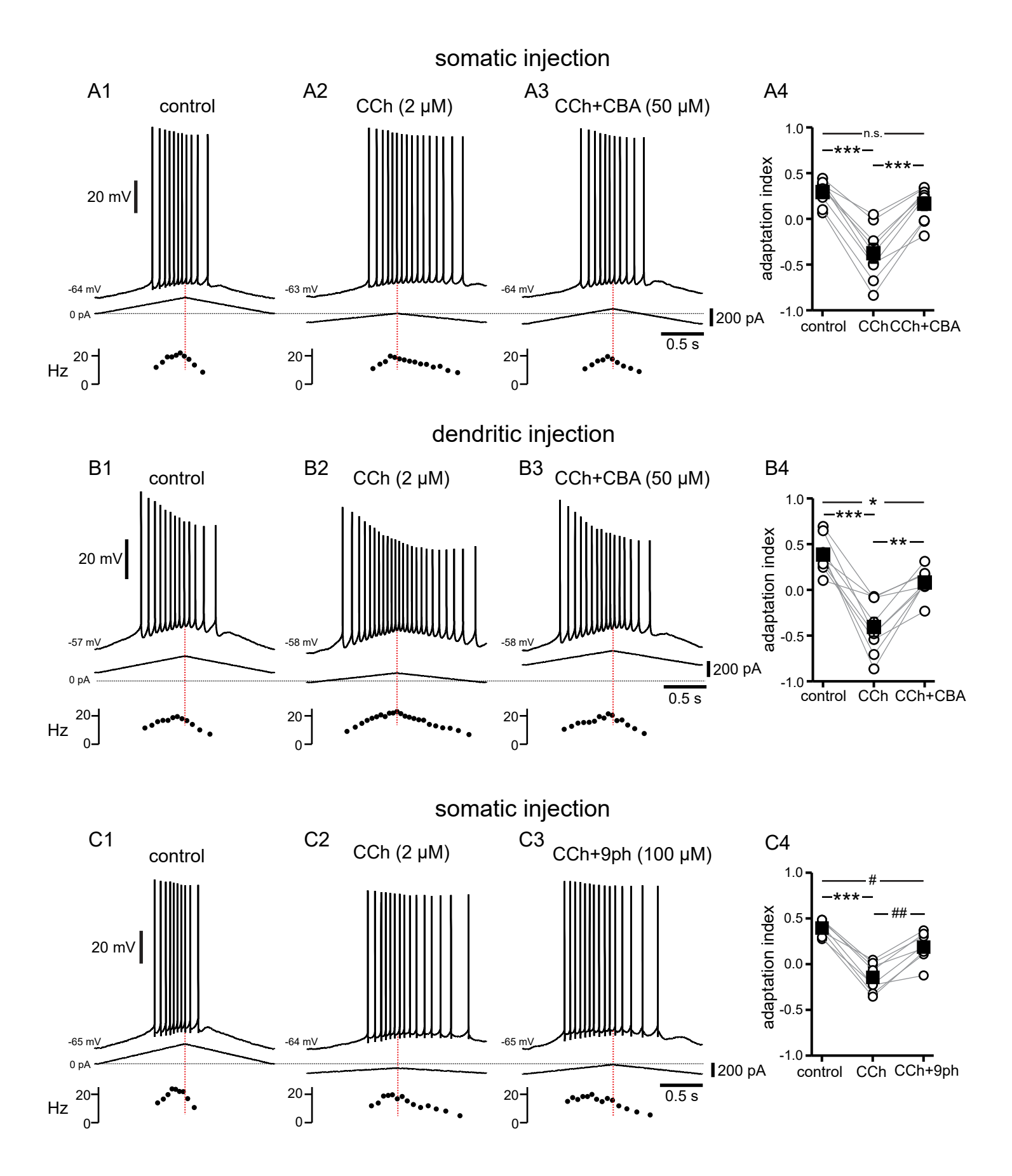


Figure 5

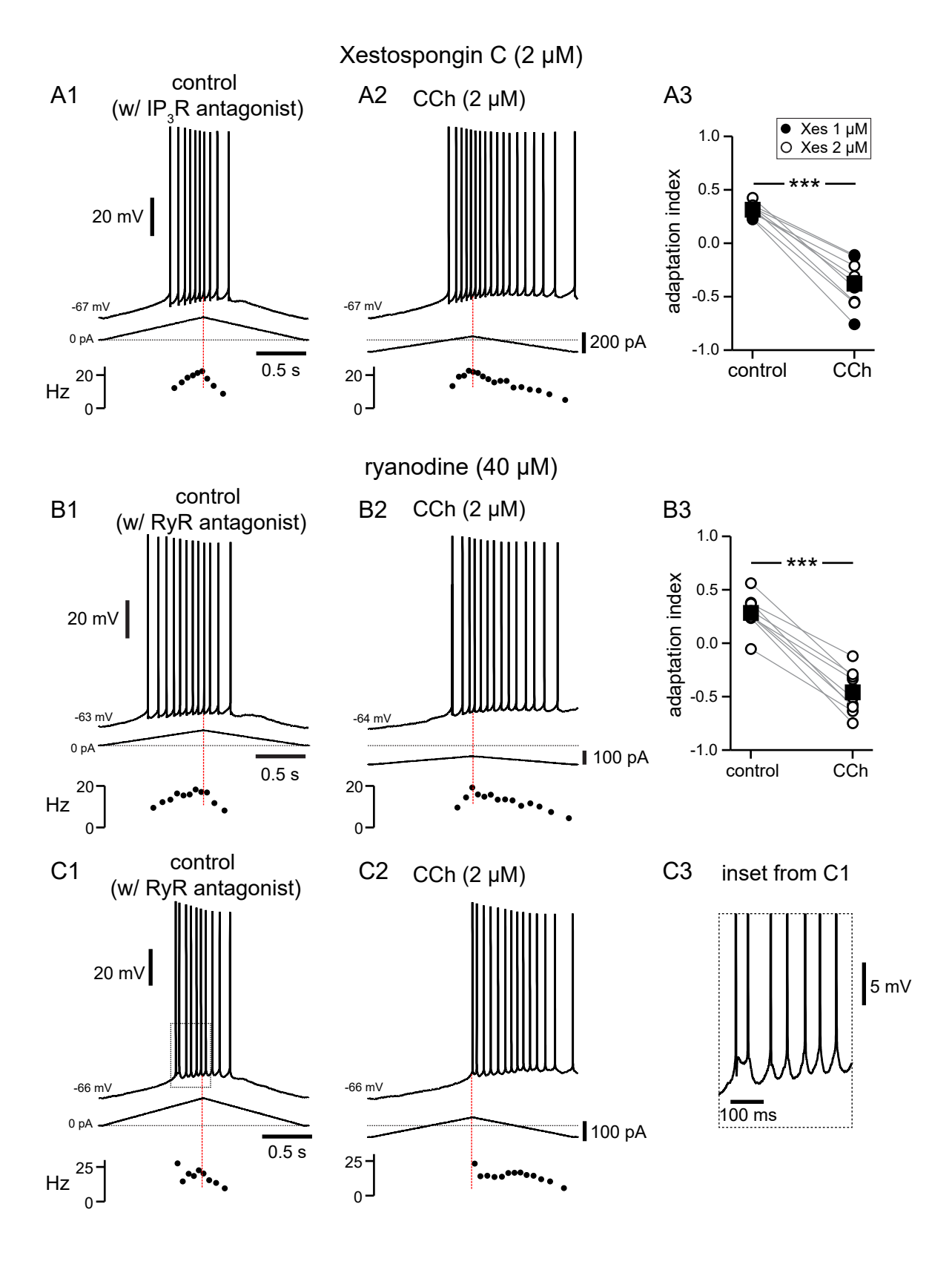


Figure 6

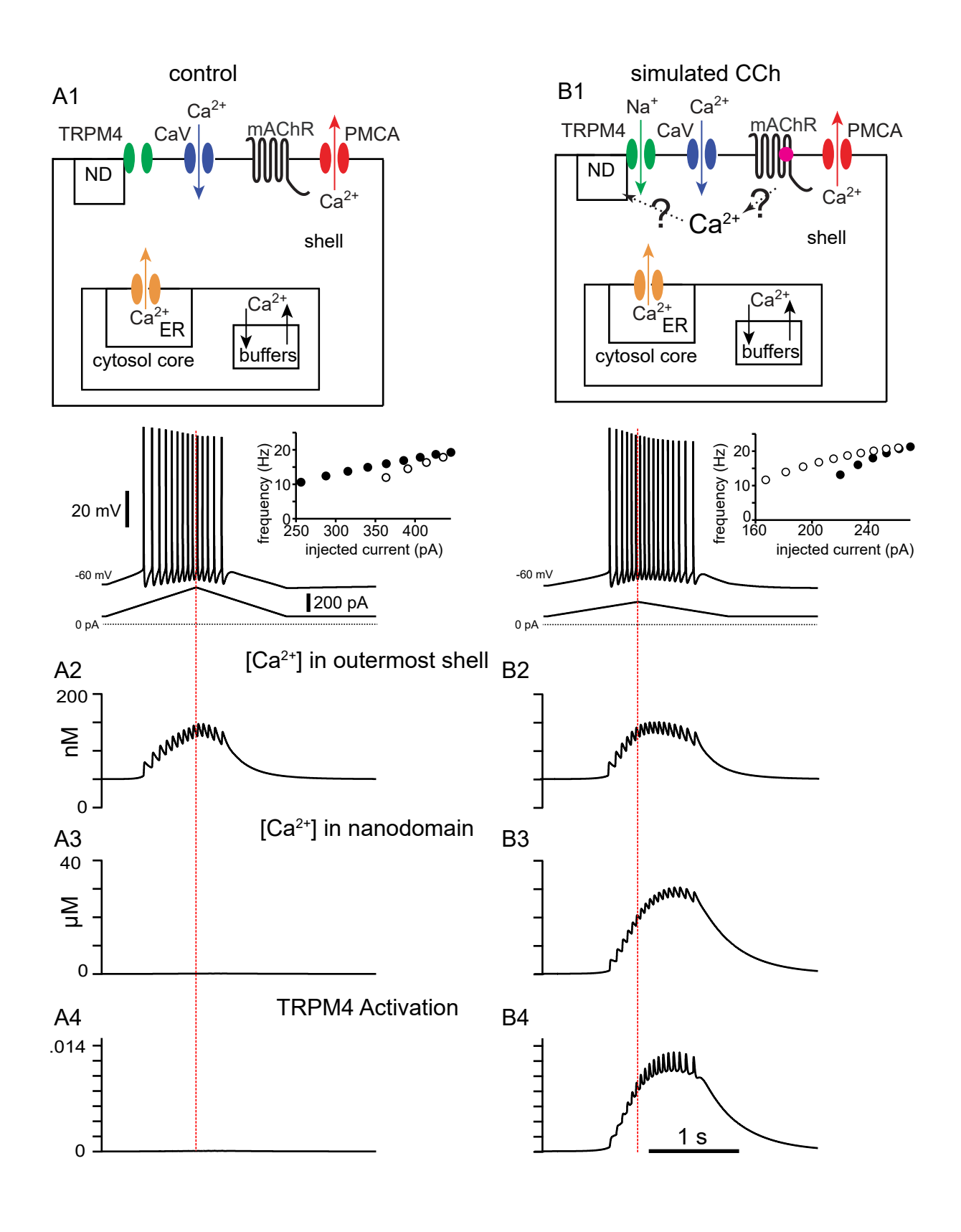


Figure 7

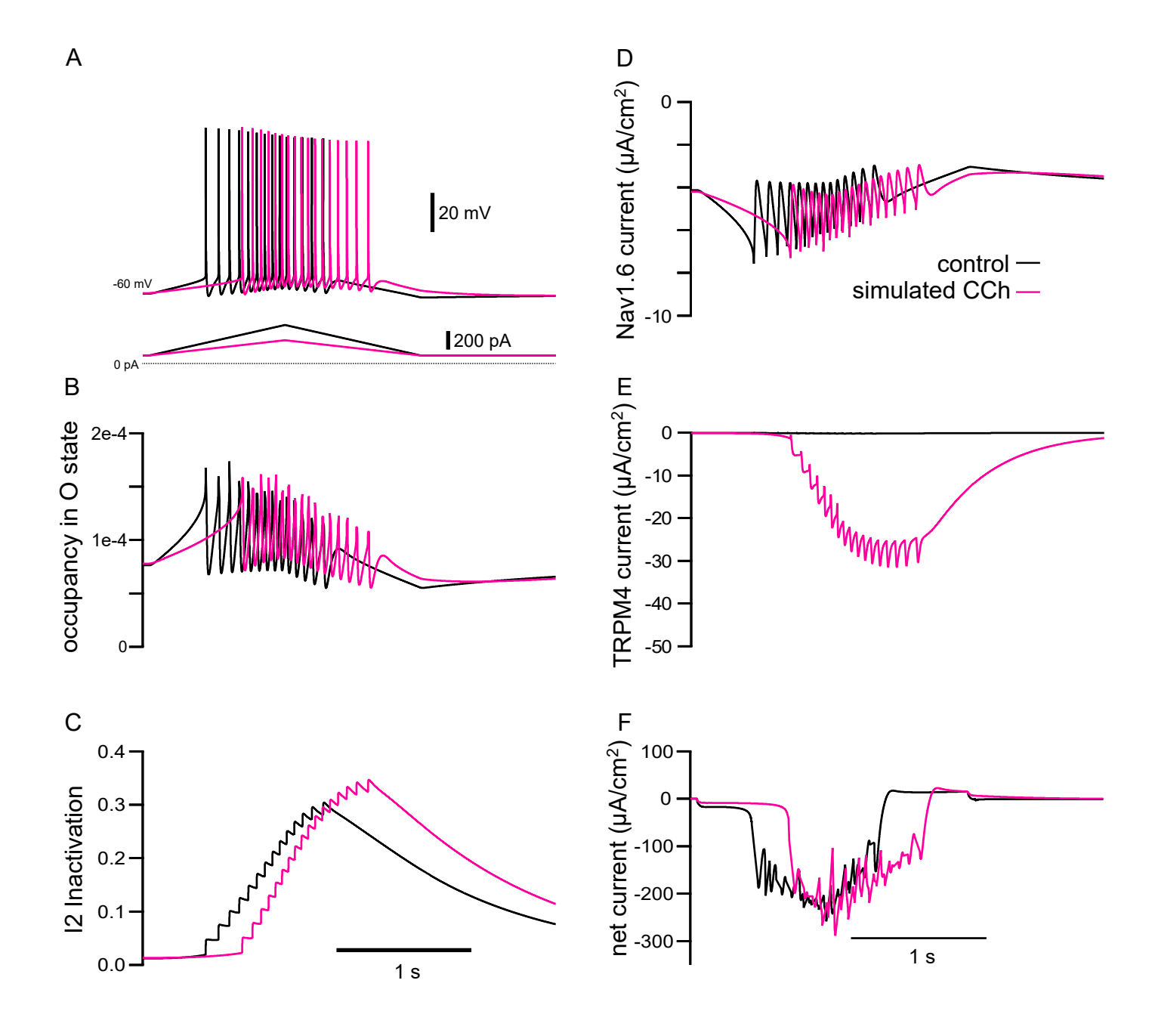


Figure 8

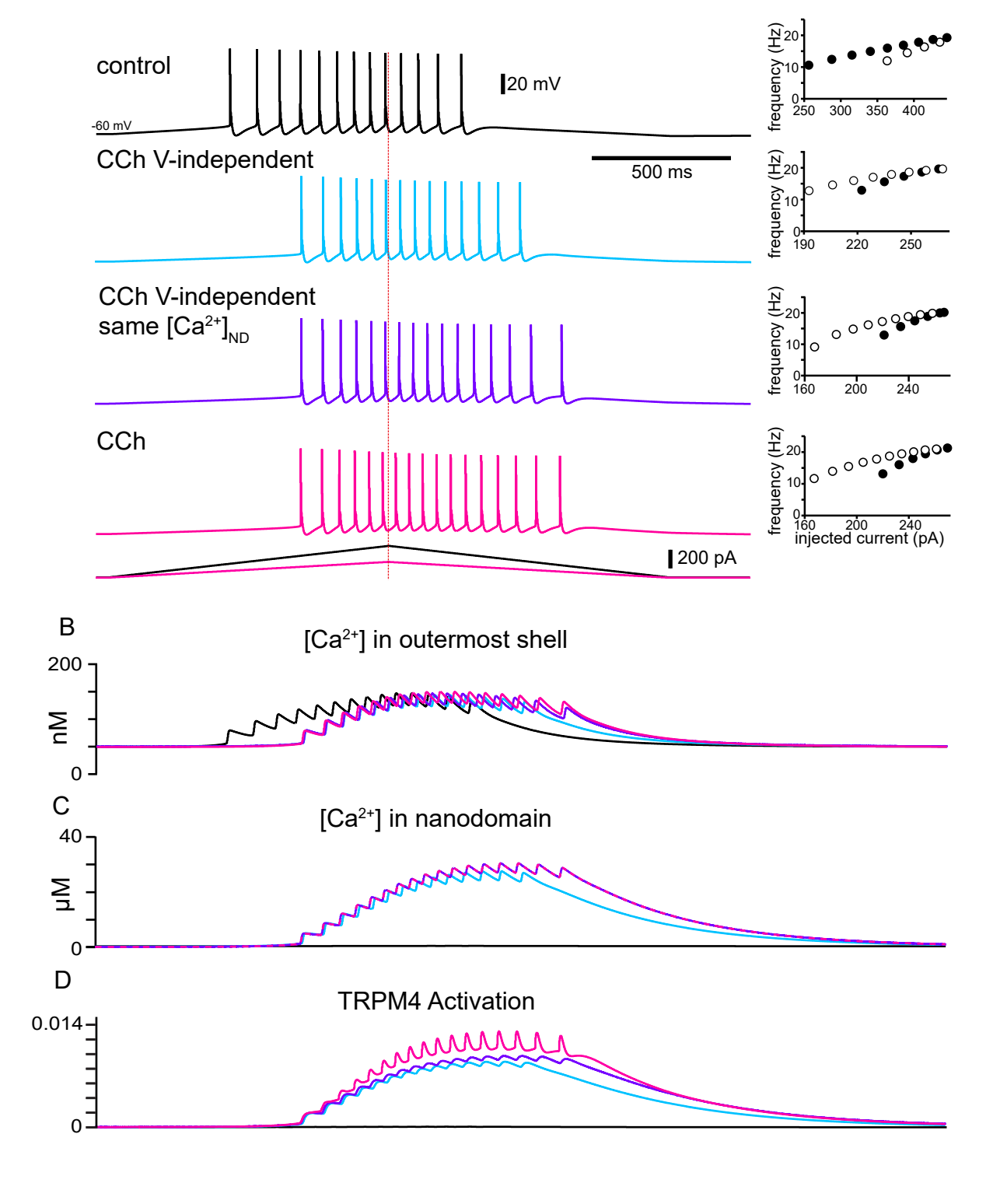
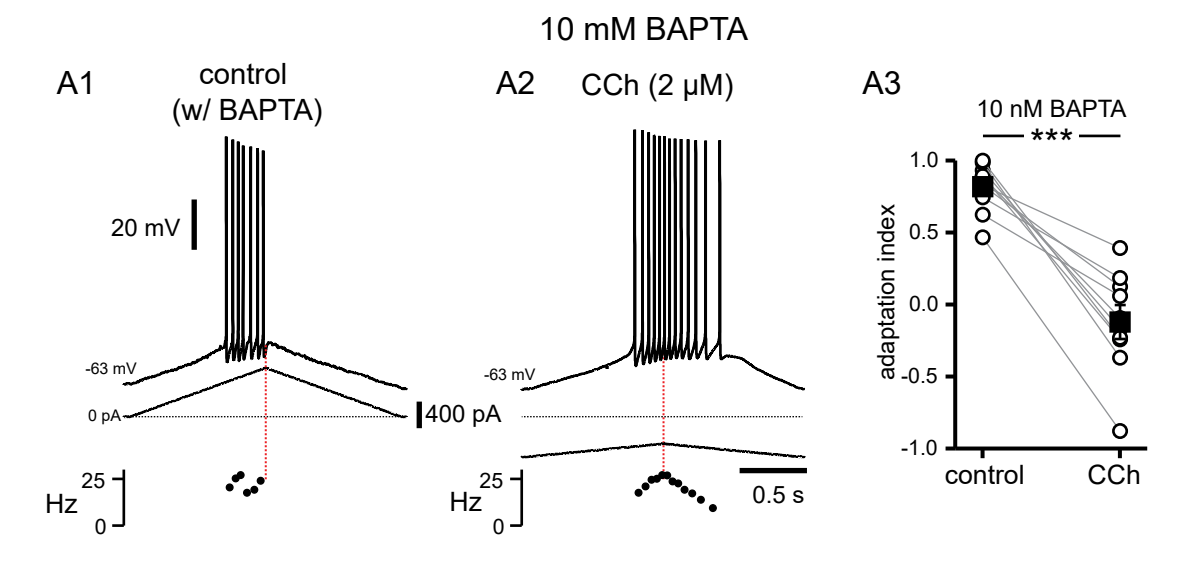
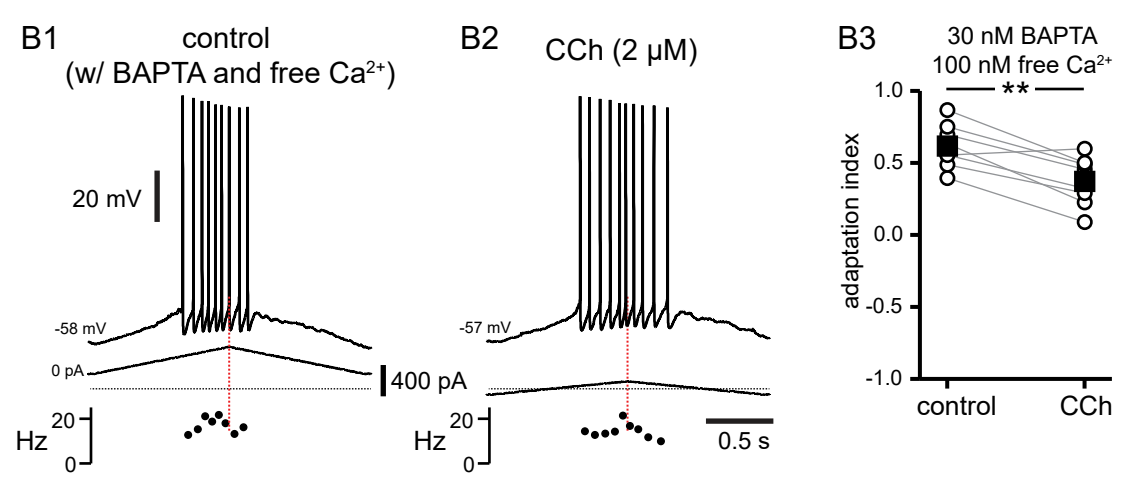


Figure 9



30 mM BAPTA and 100 nM free Ca2+



30 mM BAPTA and 10 nM free Ca2+

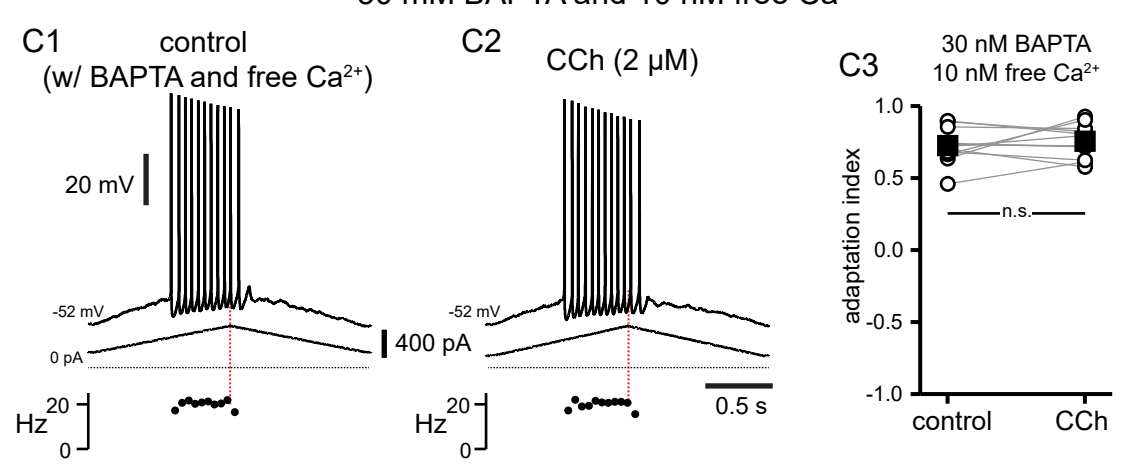


Figure 10

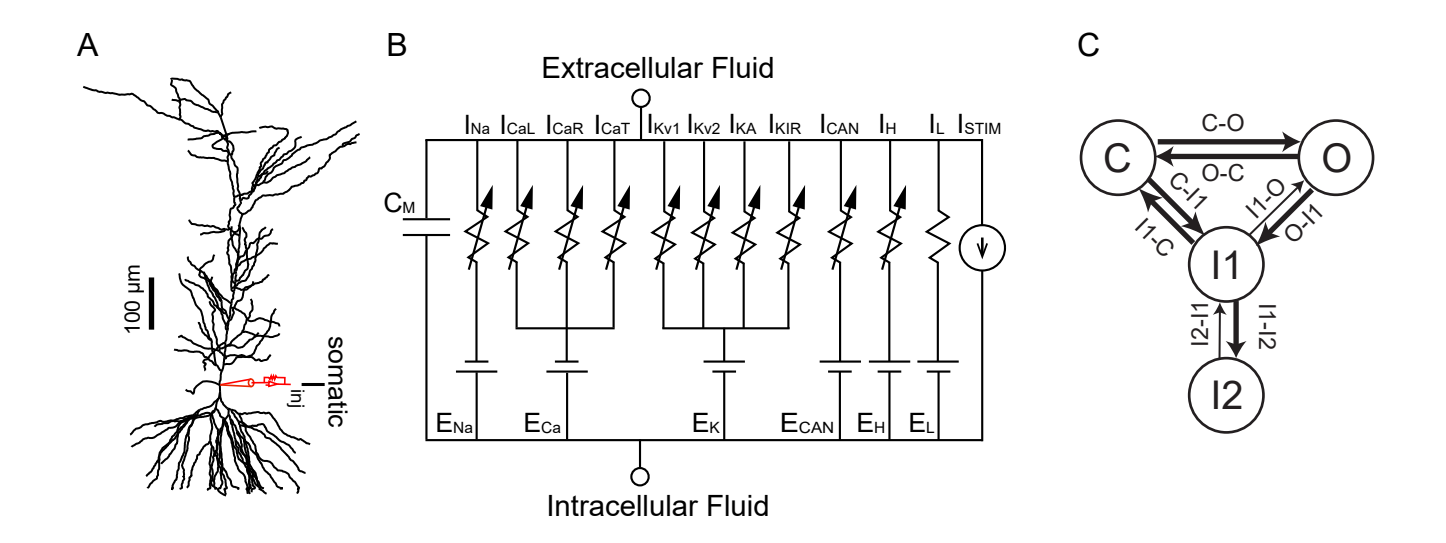


Figure 11

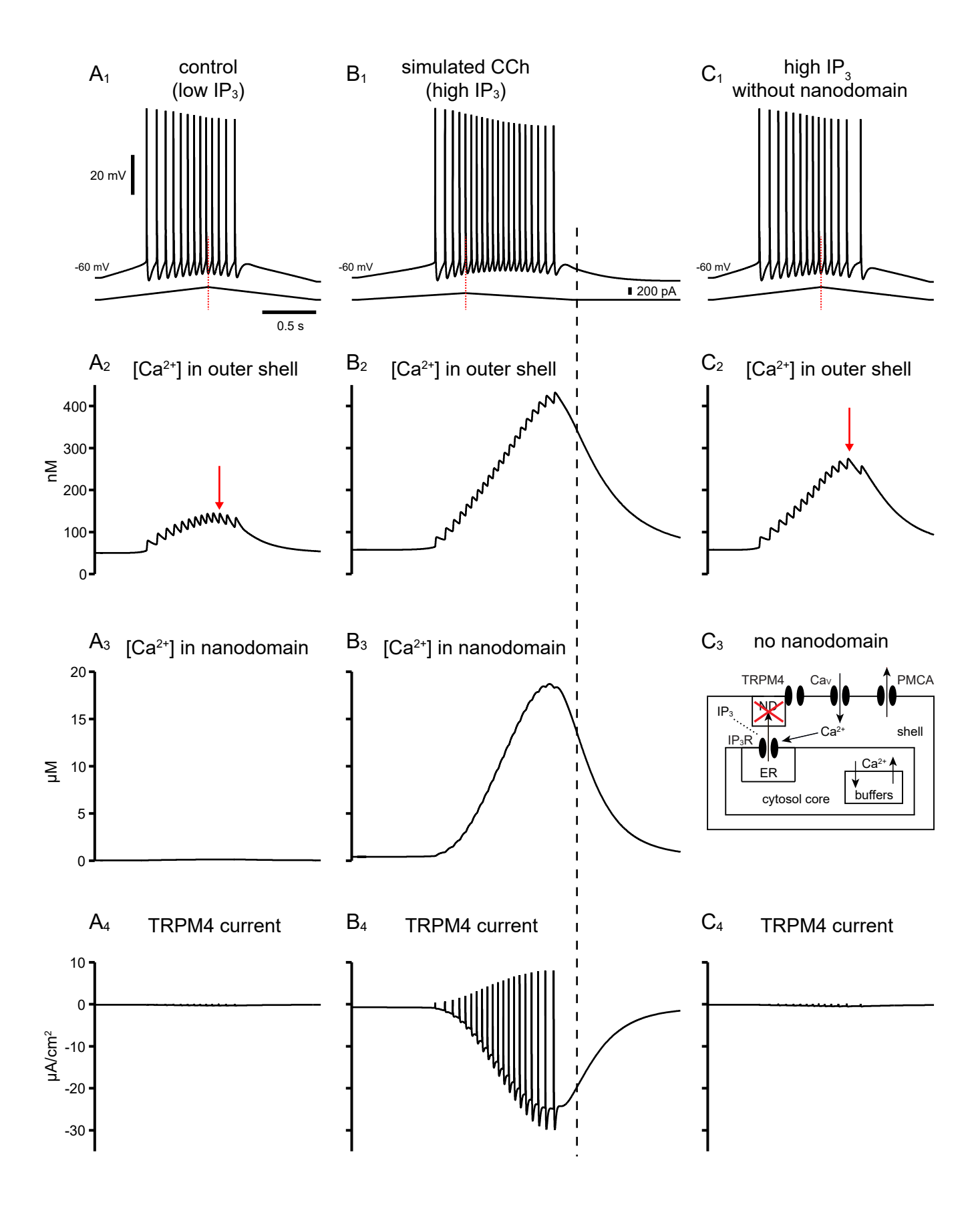


Figure 11 Supplement 1